Spatial and temporal evolution of a microseismic swarm induced by water injection in the Arkema-Vauvert salt field (southern France)

M. Godano, Th. Bardainne, M. Regnier, Anne Deschamps, M. Valette

Geophysical Journal International

Geophys. J. Int. (2012) **188,** 274–292 doi: 10.1111/j.1365-246X.2011.05257.x

Spatial and temporal evolution of a microseismic swarm induced by water injection in the Arkema-Vauvert salt field (southern France)

Maxime Godano,[1] Thomas Bardainne,[2] Marc Regnier,[1] Anne Deschamps[1] and Marc Valette[3]

[1] *Géoazur, Université de Nice-Sophia Antipolis-CNRS-IRD-OCA;* 250 *Rue Albert Einstein,* 06560 *Valbonne, France. E-mail: godano@geoazur.unice.fr*
[2] *Magnitude SAS; Centre Regain, Route de Marseille,* 04220 *Sainte-Tulle, France*
[3] *Arkema; Mas de Parrapon,* 30600 *Vauvert, France*

Accepted 2011 September 30. Received 2011 September 30; in original form 2010 October 13

SUMMARY

This study investigates a microseismic swarm induced by injection operations in the Arkema-Vauvert salt field. The seismic activity in this field is monitored only by two permanent 3-component stations deployed in two wells. This study focuses on a period of 21 months (2004 January–2005 September) during which 1214 seismic events are located. The seismic activity is divided into three periods correlating with the water injection operations, highlighting a migration of the seismicity toward a thrust fault connecting the injection well and the production well. A waveform analysis reveals *S*-wave anisotropy, and focal mechanisms are computed using *P, Sv* and *Sh* amplitudes manually measured on anisotropy-corrected seismograms. First, synthetic resolution tests assess the reliability of the focal mechanisms determination from the two 3-component stations deployed in the field. Synthetic data are generated for 1056 earthquakes with various focal mechanisms and are perturbed with noise. The results indicate that the type of focal mechanism is correctly retrieved for 74 per cent of the synthetic earthquakes, but the uncertainties of the strike and rake are significant (from 15 to 45°). Next, the focal mechanisms are computed for 532 real earthquakes. The solutions primarily correspond to a dip-slip/thrust fault type with subvertical NE–SW and subhorizontal N–S to NW–SE nodal planes. Correlations between the focal mechanisms and the spatio-temporal distribution of the seismic activity are noteworthy. The study shows it is possible to reliably retrieve double–couple focal mechanisms for some faulting geometries with two 3-component seismological stations. However, the reliability of the focal mechanism retrieval depends on the station configuration. Therefore, the addition of further stations would improve the results.

Key words: Downhole methods; Hydrogeophysics; Fracture and flow; Earthquake source observations.

1 INTRODUCTION

In the last 15 years, seismological monitoring of reservoirs has steadily increased. The potential applications of this monitoring are numerous (Maxwell & Urbancic 2005). In reservoirs, seismicity is directly induced by various operations carried out at the well or intrawell scale, including fluid injection or extraction (Phillips *et al.* 2002). Due to low-to-very low magnitudes (generally $M_w \leq 0$), this seismic activity is conventionally named microseismicity. However, the classification of the seismicity is an ongoing discussion, and more detailed classification for the earthquakes with magnitudes lower than three has been proposed (e.g. Bohnhoff *et al.* 2010). In the reservoir context, one very common monitoring network consists of a set of sensors deployed in wells to decrease the magnitude detection threshold, improve the signal-to-noise ratio and thus increase the sensitivity. Such a design has two main consequences: (1) it often depends on the availability of existing wells, and (2) the deployment cost is high. These factors limit the number of sensors used for such surveys.

Such minimalistic seismological networks greatly limit the study of seismicity. The determination of the double–couple (DC) focal mechanism (fault plane solution) using the *P*-wave polarity (e.g. Reasenberg & Oppenheimer 1985; Hardebeck & Shearer 2002) is particularly sensitive to the small number of stations. This implies the use of more robust alternative methods constraining the fault plane solution, such as the inversion of the direct-wave amplitudes (e.g. Snoke 2003; Hardebeck & Shearer 2003; Godano *et al.* 2009) or the waveform (e.g. Langston 1982; Delouis & Legrand 1999).

Nevertheless, the fault plane solution does not resolve non-DC rupture processes that can occur in water-injection contexts including reservoirs. The resolution of the non-DC processes requires the determination of six independent elements of the general moment tensor (e.g. Stump & Johnson 1977; Dziewonski *et al.* 1981; Sipkin 1987). The determination of these six parameters requires more observations than the determination of the three parameters in the DC fault plane solution.

This paper studies the seismicity induced by water injections in the Arkema-Vauvert salt field in southern France. In this field, the seismic activity is monitored by two 3-component sensors deployed in two wells. This network configuration approaches the study of microseismic activity in the reservoir context from an extreme minimalist position. Through this paper, we illustrate the type of information provided by the microseismicity recorded by this type of network and indicate the limitations to a detailed understanding of the fracturing process in the reservoir.

A preceding study of the Arkema-Vauvert seismicity (Godano *et al.* 2010) focused on the source parameters and focal mechanism of some events recorded in the field. In this paper, we focus on the spatio-temporal variability of a microseismic swarm (1200 events during 21 months) induced by the exploitation of Wells PA22 and PA23 in the NE portion of the field. In the first part of our study, we present the geology and the microseismic activity of the Arkema-Vauvert salt field. In the second part, we analyse the locations, the waveform and the fault plane solutions of the earthquakes induced by the exploitation of the wells PA22 and PA23. Finally, in the third part, we discuss the obtained results and the limitations caused by the minimalistic seismological network configuration.

2 THE ARKEMA-VAUVERT SALT FIELD

2.1 Geological setting and exploitation

The Arkema-Vauvert salt field is located on the NW margin of the Camargue basin in southeastern France (Fig. 1) and results from the Oligo-Aquitanian rifting (e.g Séranne *et al.* 1995). This basin is bounded by the major extensional, SE-dipping Nîmes fault and contains more than 4000 m of syn-rift sediments that overlay Mesozoic carbonates and are covered by transgressive Burdigalian marine sediments (16–20 Myr) (Valette & Benedicto 1995).

The Arkema-Vauvert salt formation, located at a depth between 1900 and 2800 m, consists of approximately 50 per cent salt rock and 50 per cent insoluble material (anhydrite and clay). This salt formation is divided into three series (Valette & Benedicto 1995) (Fig. 2):

(1) the autochthonous salt series affected by NW-dipping normal faults (Oligocene extension);

(2) the lower allochthonous salt series separated from the autochthonous series by the D1 thrust fault and

(3) the upper allochthonous salt series separated from the lower allochthonous series by the D2 thrust fault and affected by the

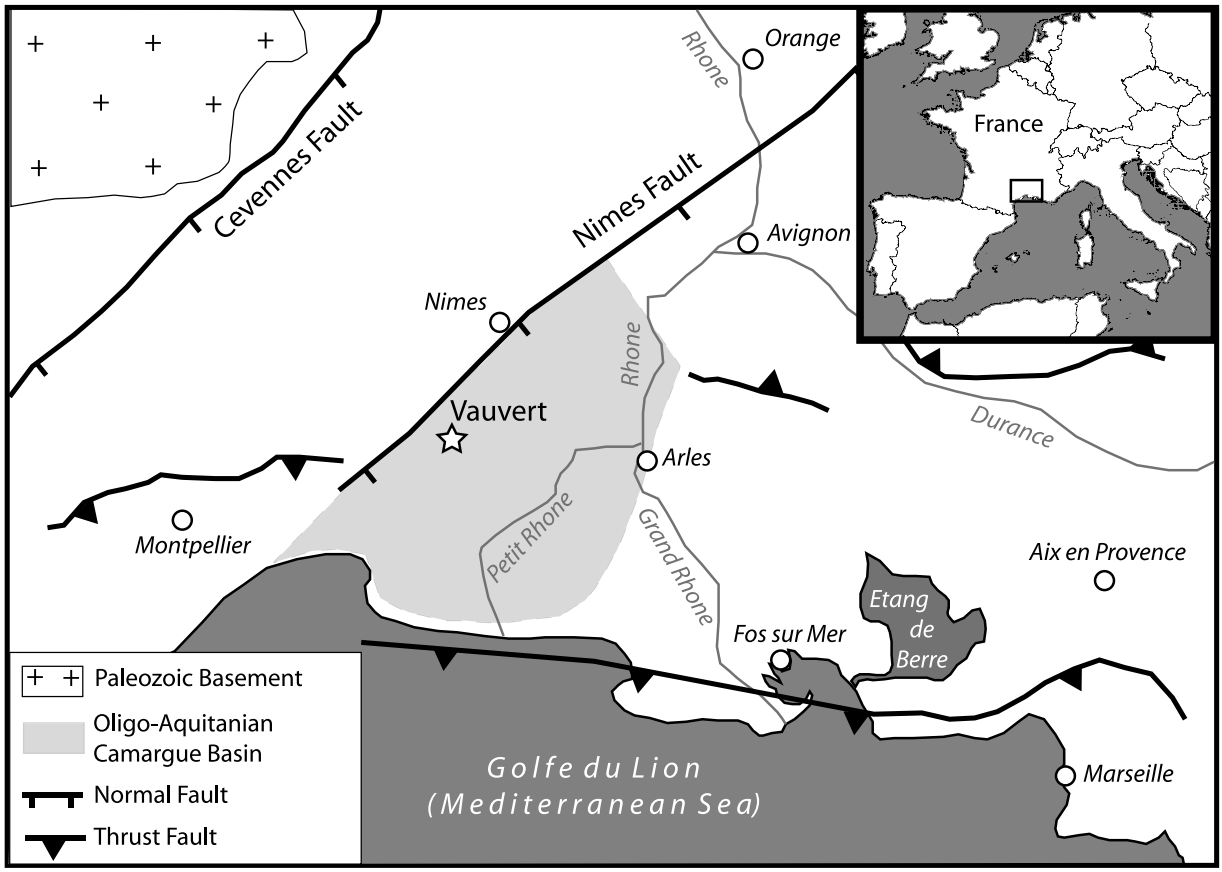

Figure 1. Map of Western Europe (inset) and schematic structural map of the Rhone delta region (South-eastern France). The Arkema-Vauvert salt field is located in the Oligo-Aquitanian Camargue basin and is bounded by the extensional SE-dipping Nîmes fault.

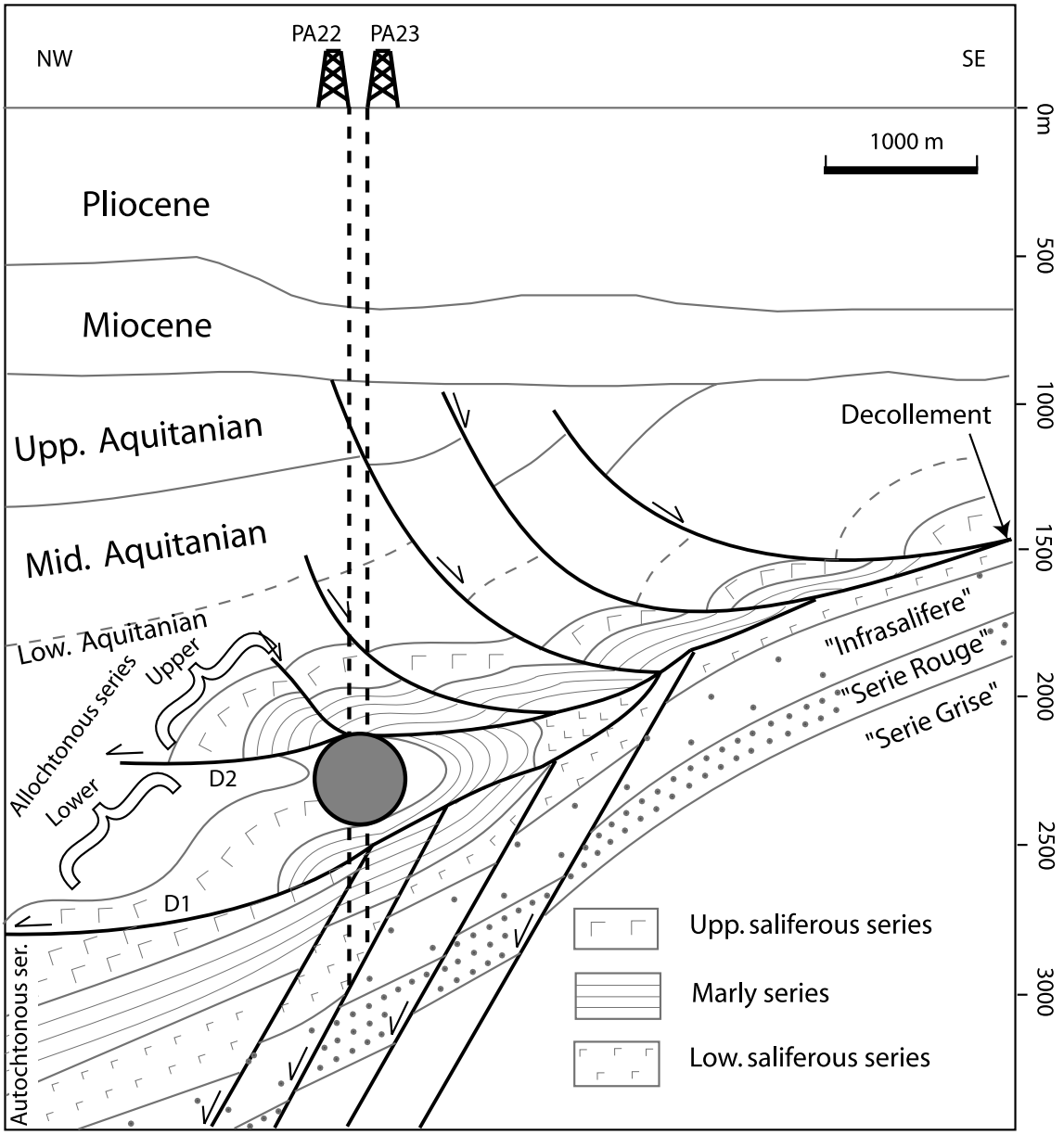

Figure 2. Geological cross-section of the Arkema-Vauvert salt field. The salt formation is divided in three series: the autochthonous salt series and the lower and upper allochthonous series. The grey circle indicates the target area for the water-injection operations at Wells PA22 and PA23 [modified from Valette & Benedicto (1995)].

SE-dipping listric normal faults that accommodate the extension from the upper Aquitanian series.

For 30 years, the salt formation has been exploited by the Arkema Company. The production process consists of dissolving salt by circulation of fresh water (solution mining) through fracture zones between one injection well and one production well (doublet; Fig. 3) or one injection well and two production wells (triplet). The produced brine is then piped to chemical plants at Etang de Berre and Fos sur Mer, near Marseille.

Solution mining creates cylindrical cavities about 30 m in diameter and 500 m high. After brine production ceases, the cavities are filled with brine. A creeping phenomenon tends to reduce the size of the caverns and induces subsidence. The monitoring of ground deformation by radar interferometry between 1993 and 1999 revealed a subsidence velocity of approximately 2.2 cm yr^{-1} over an area with a 4 km radius (Raucoules *et al.* 2003).

2.2 Microseismic activity of the Arkema-Vauvert salt field

The decrease in cavity size also increases the pressure of the brine, and this fluid overpressure produces and propagates fractures between wells, inducing abundant microseismic activity (interdoublets activity) (Maisons *et al.* 1997). Freshwater injection during the mining solution process induces intradoublet activity, another type of microseismic activity. For safety concerns, the authorities have requested seismic activity monitoring to anticipate fracture propagation toward the surface and salt contamination of the Burdigalian (Miocene) aquifer at a 900 m depth. The seismological network is composed of two 3-component, 28 Hz velocimeters anchored in

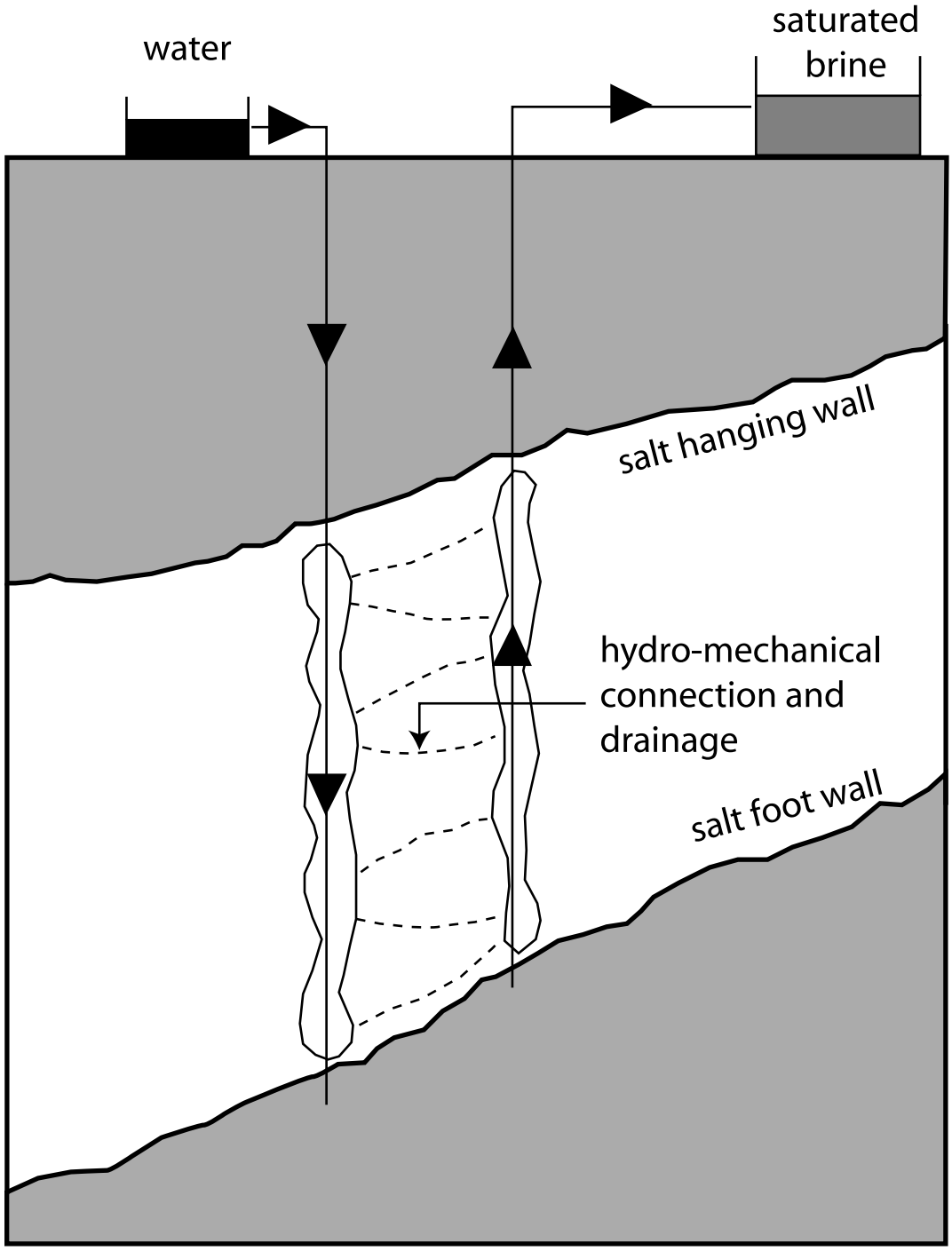

Figure 3. Schematic diagram displaying the salt exploitation process. Water is injected in the salt formation by an injection well, drains along fractures and dissolves the salt. A second well extracts the resultant brine [modified from Maisons *et al.* (1997)].

the PA7 well (Sensor M0) and PA9 well (Sensor M1) at 1400 and 1800 m, respectively (Fig. 4). The data are recorded with a sampling rate of 2400 Hz, and signal-to-noise ratios are typically greater than 5.

In practice, the events recorded by this network are located using only the deeper sensor (M1) because the velocity model between the cluster and this sensor is better understood than that between the cluster and Sensor M0. This single-station location process requires the use of *P*-wave polarization angle (azimuth and takeoff angle) in addition to the *P* and *S* arrival times. The polarization is computed from the particle motion of a signal-window immediately after the observed *P*-wave arrival on the 3-component receiver (e.g. Aster *et al.* 1990), and the distance to the sensor is given by the *S–P* time and the velocity model (Table 1). Because only one sensor is used for location, no uncertainty consideration can be made. We can only estimate error using an estimation of time and polarization measurement errors and velocity model uncertainty.

The limited number of geophysical investigations of this field allowed building a simple velocity model that does not account for lateral velocity variations. This model consists of the three

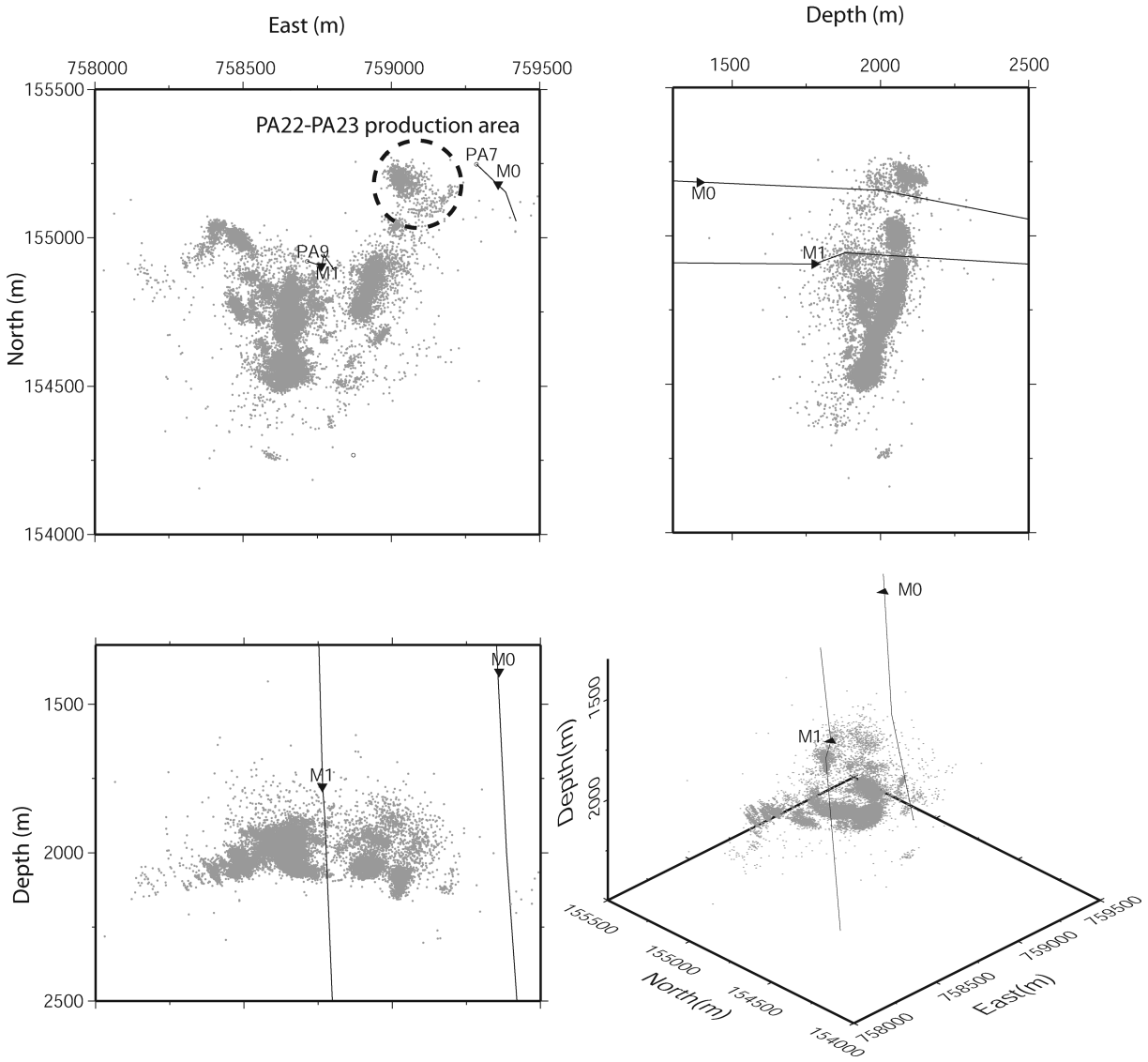

Figure 4. Plan view, N–S and E–W cross-sections and 3-D view of the Arkema-Vauvert salt field showing the position of the permanent seismological stations (M0 and M1), the microseismic activity recorded in 2008 and the production area of the PA22 and PA23 wells [modified from Godano *et al.* (2010)].

Table 1. One-dimensional velocity model used in the Arkema-Vauvert salt field. The ratio between V_p and V_s equals 1.7.

Depth (m)	V_p (m s^{-1})	V_s (m s^{-1})
0–1800	3700	2176
1800–2170	4400	2588
2170–∞	4000	2353

horizontal layers described in Table 1. This may appear contradictory to the geological complexity and to the damage caused by solution mining to the rocks over time. In addition, the presence of the brine-filled cavities may mask some seismic phases. However, the damaged zones are narrow, and we assume that the wavefield is only slightly perturbed. Moreover, the variations of the medium properties are accounted for using regular optimization of the velocity model with calibration shots performed in the field. These shots are also used to orient the three components of each tool. With such a model and the measurement uncertainties (times and polarization), the location uncertainty is approximately 6 to 8 per cent of the source-tool distance (typically 40–60 m for 600–700 m average source-tool distance).

More than 125 000 events have been located between 1992 (starting monitoring date) and the end of 2007. The moment magnitude of these events ranges from −3 to −0.5. Since 2004, the microseismic activity pattern changed little, as illustrated in Fig. 4 which displays the seismicity during 2008. The seismicity is intensive in the central part of the field where production has halted (interdoublet activity). At the periphery, seismicity occurs at the doublets in production (PA22–PA23) and corresponds to intradoublet seismic activity.

3 MICROSEISMIC ACTIVITY AT THE PA22–PA23 DOUBLET

The brine production at the PA22–PA23 wells doublet began in 2003 April. The dissolution area is the lower allochthonous salt series under the D2 thrust surface. We focus on the seismic activity

induced at this doublet during a period of 21 months (from 2004 January to 2005 September).

3.1 Location of the microseismic events

During the 21-month period, 1214 events were located (Fig. 5), exhibiting a notable diffuse aspect related to the single station location. Fig. 6 reports the pressure variations of the PA22 and PA23 wells and the number of earthquakes detected during the 21 months. The analysis of this graph outlines three main periods:

(1) Period 1 occurs between 2004 January and September. Until 2004 March 15, PA23 is the water-injection well (under pressure), and PA22 is the brine production well. After March 15, pressure drops suddenly at PA23 and increases at PA22. This corresponds to an inversion performed by the operators between the injection and the production wells. PA22 then becomes the injection well, and PA23 becomes the production well. One month later, pressure drops at PA22, correlating with a slight increase of the seismicity rate. This pressure drop implies a hydraulic connection with PA23 along fractures. The increase of the seismicity rate following the pressure drop indicates that fluid circulation induces seismic ruptures on these fractures. During Period 1, the seismicity is located in the lower allochthonous salt series (dissolution area) (Fig. 5a). Thus, the connection between PA22 and PA23 is probably made along fractures located under the D2 thrust fault. In addition, a migration of the seismicity in time toward the D2 thrust fault apparently occurs.

(2) Period 2 starts on 2004 September 27 and includes a second inversion performed by the operators between the injection and the production wells, in which P23 becomes the injection well. A sudden pressure drop at PA23 follows the inversion, correlates with a significant increase in the seismicity rate (minor seismic crisis) and indicates an important hydraulic connection between PA22 and PA23. The seismic events are primarily located around the D2 thrust fault (Fig. 5b); therefore, the hydraulic connection could be made along this structure.

(3) Period 3 begins at the end of 2004 October with a pressure decrease at PA23. Numerous other pressure decreases at PA23 are observed and correlates with a major seismic crisis around the D2

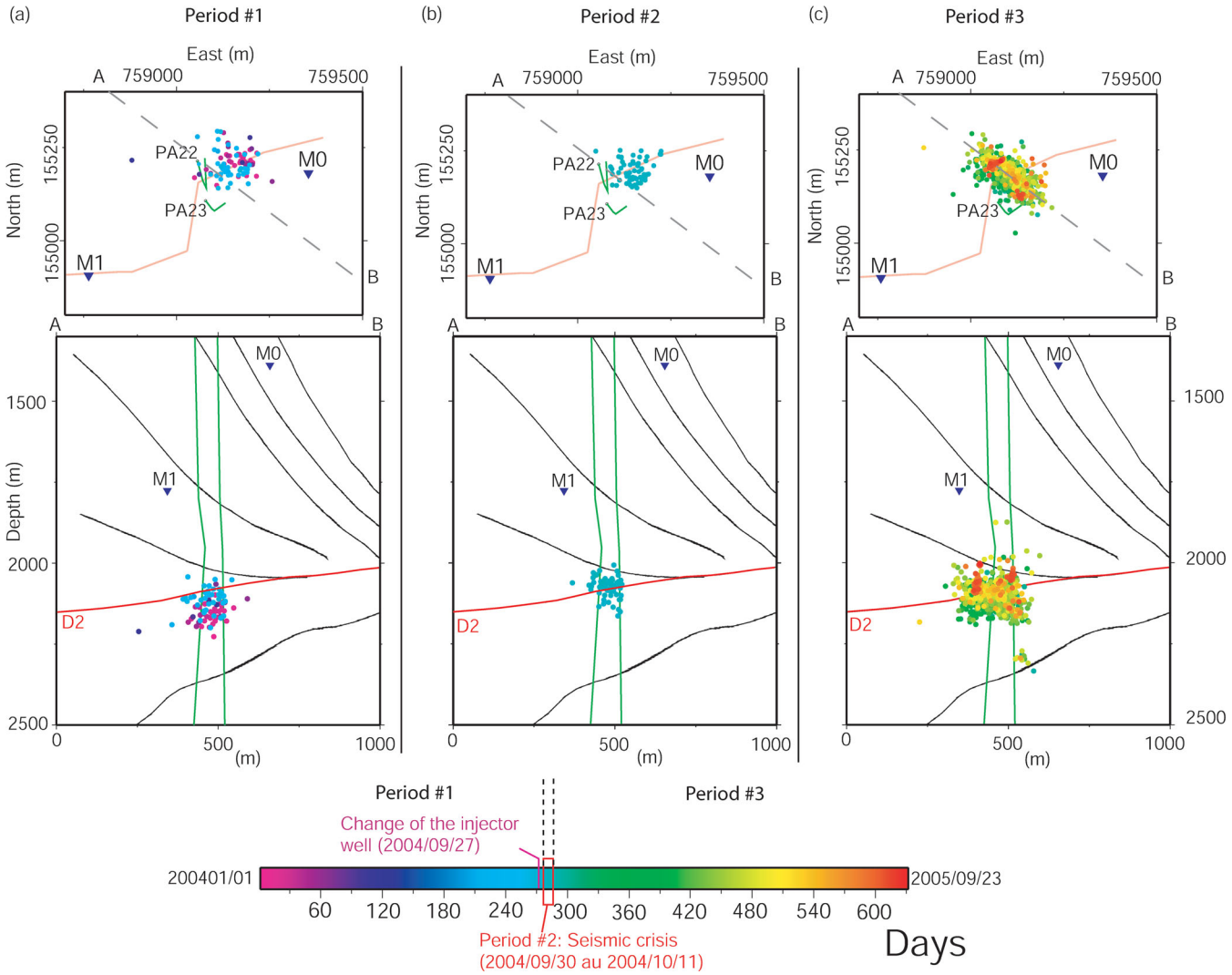

Figure 5. Spatial and temporal evolution of the seismicity induced by the exploitation of the PA22–PA23 doublet. The seismic activity is divided in three periods. Period 1 (2004 January–September) is characterized by a seismicity located in the lower allochthonous salt series. Period 2 (2004 September–October) is characterized by a seismic activity located at the depth of the D2 thrust fault. Period 3 (2004 October–2005 September) is characterized by a seismicity around the D2 thrust fault and in the lower allochthonous salt series. The colour of the earthquakes corresponds to the colour of the timescale.

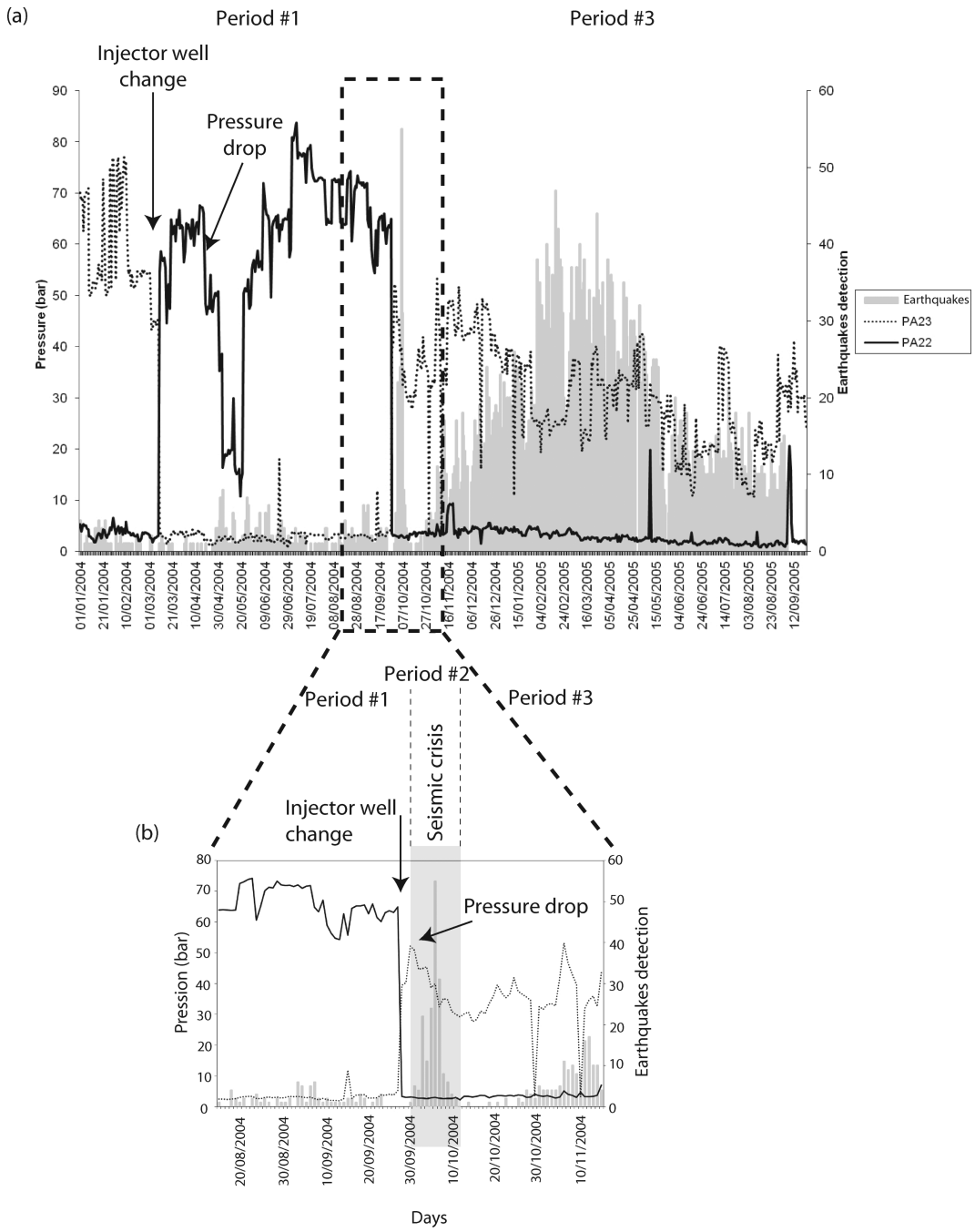

Figure 6. (a) Pressure diagram of the PA22 and PA23 wells and detected seismic events during the 21-month period (2004 January 1–2005 September 29). (b) Zoom around Period 2 (2004 August 15–2004 October 15). The inversions performed by the operators between the injection and production wells and the pressure drops are indicated by arrows.

fault and in the lower allochthonous series (Fig. 5c). The seismicity rate reaches its maximum at the end of 2005 February. At the end of Period 3 in 2005 August, the seismicity is limited to two areas near D2 and highlighted by small earthquake clusters (red in Fig. 5c).

3.2 Waveform analysis

Fig. 7 displays examples of the 3-component velocity records at the M0 and M1 stations for two earthquakes. These seismograms are rotated to maximize the energy of the *P*-, *Sv*- and *Sh*-waves on each component using *P*-wave polarization analysis. The covariance matrix is first calculated in a manually determined temporal window corresponding to the first period of the direct *P*-wave with a typical length ranging between 6 and 8 ms. The eigenvectors and eigenvalues of this matrix are then computed. The eigenvector corresponding to the largest eigenvalue is the vector of the direction along which the *P*-wave energy is maximized, that is, the direction of the *P*-wave at the station (polarization vector **L**). The polarization vector of the *Sh*-wave (**T**) is obtained as the cross-product between the vector of the vertical direction and the polarization vector of the *P*-wave. Similarly, the polarization vector of the *Sv*-wave (**R**)

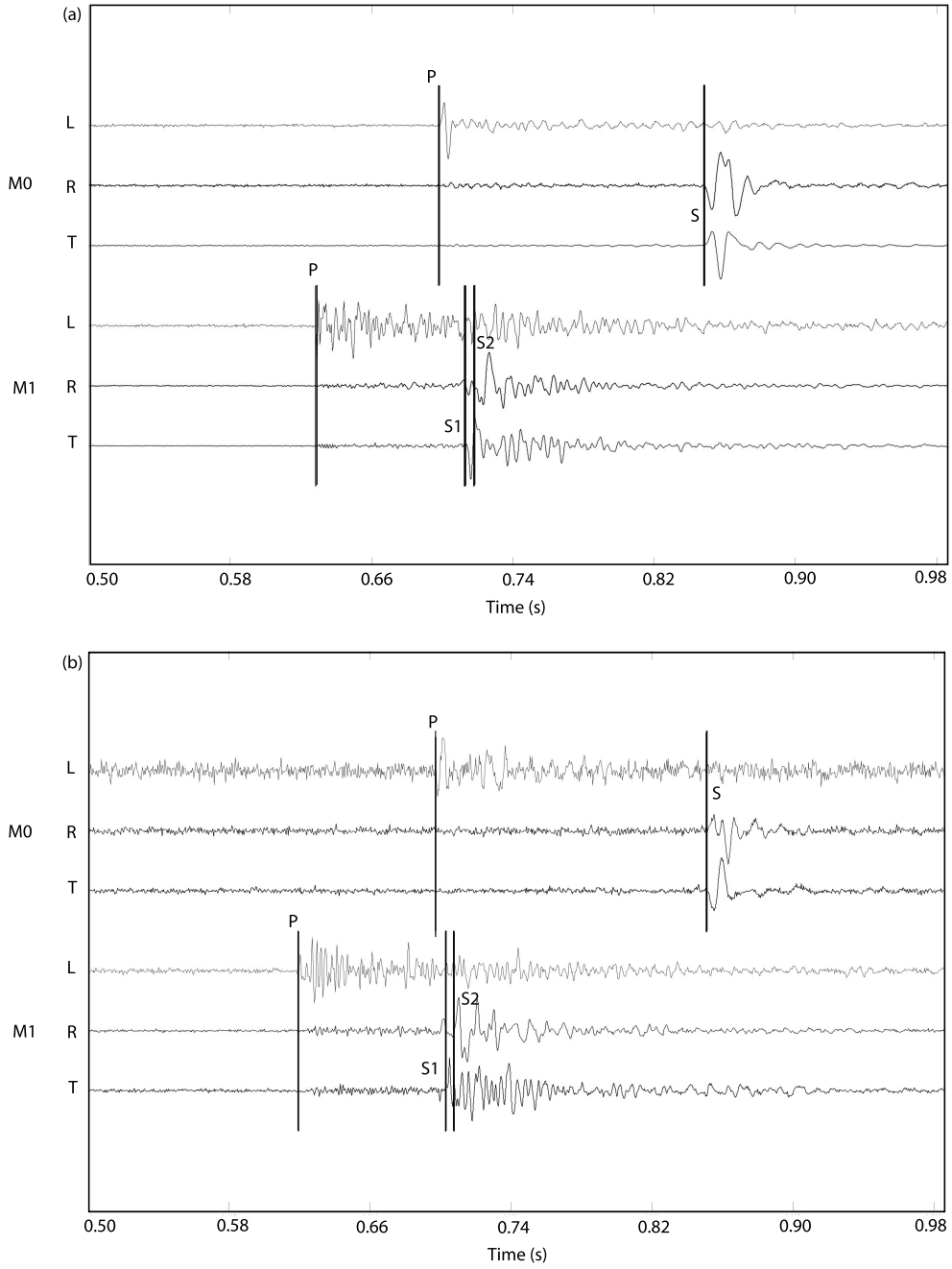

Figure 7. Examples of 3-component velocity records rotated in the longitudinal (**L**), radial (**R**) and transverse (**T**) coordinates. (a) A seismic event recorded 2004 September 3 at 11:30:44 ($M_w = -1.53$), and (b) a seismic event recorded 2005 February 6 at 07:44:29 ($M_w = -2.55$).

is given by the cross-product of (**T**) and (**L**). The concatenation of these three polarization vectors gives the rotation matrix applied to the 3-component seismograms.

The analysis of the rotated seismograms clearly reveals *S*-wave anisotropy at Station M1, in two separated phases, S1 and S2 on the **T** and **R** components, which correspond to the fast and slow *S* waves, respectively. The slow and fast *S* phases are clearly separated because their polarization vectors are near the polarization vector of the *Sv*- and *Sh*-waves, respectively. On the other hand, anisotropy is less visible at Station M0. Nevertheless, we observe a complex waveform in the **R** component, characteristic of a poor separation between the slow and fast *S*-waves. The polarization vectors of the slow and fast *S*-waves differ from the polarization vectors of the *Sv*- and *Sh*-waves. The greater delay time between slow and fast *S*-waves at Station M1 than at Station M0 probably indicates a high fracture density between the seismic swarm and Station M1.

Due to anisotropy, the *Sv*- and *Sh*-amplitudes measured on the **R** and **T** components of the rotated seismograms are erroneous because they correspond to the vectorial sum between the slow and fast *S* waves. This may be problematic for the focal mechanism determination from the inversion of the direct-wave amplitudes. It is therefore necessary to correct the effect of anisotropy on the amplitudes before using them for the focal mechanism determination. The polarization angle of the fast *S* wave (ϕ) and the delay time (δt) between fast and slow *S*-waves are used to remove anisotropy in the seismograms (Ando *et al.* 1983; Silený & Milev 2008). The

parameters ϕ and δt are determined using the following method (e.g. Vlahovic *et al.* 2002; Elkibbi & Rial 2005; Tang *et al.* 2008). First, the **R** and **T** components of 300 Hz lowpass-filtered seismograms are successively rotated by 10° increments until the fast and slow *S* waves separates clearly and aligns with the **R** and **T** directions, respectively. The rotation angle giving this alignment is the polarization angle of the fast *S* wave (ϕ). The delay time δt is given by the cross-correlation between the slow and fast *S* waves (Fig. 8a). Next, the seismograms are shifted in time (Fig. 8b). Finally, the seismograms are submitted to an inverse rotation $-\phi$ to express them in the **R**–**T** coordinates (Fig. 8c). As displayed on the hodograms, this correction enables the reconstruction of the linear polarization of the *S* wave.

We correct the seismograms manually due to the advantage of checking for the correct alignment of the fast and slow *S* waves with the **R** and **T** directions. Nevertheless, this work is time-consuming, given a large number of data to correct; therefore, we only correct the seismograms of 800 events, which are randomly selected in the database of the 1214 located events. From this new database of 800 events, it was possible to correct the seismograms of 638 events.

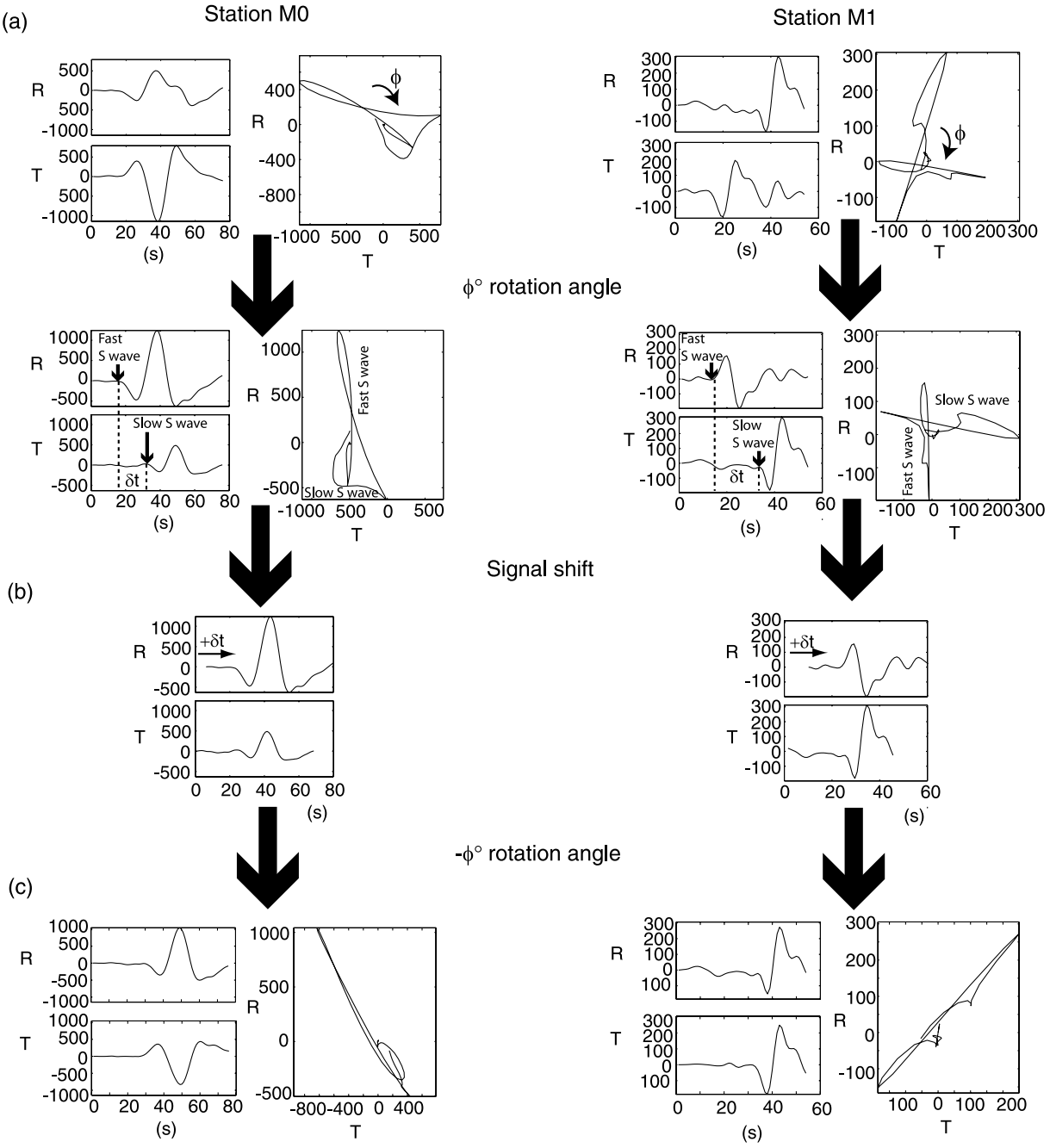

Figure 8. A schematic diagram displaying the correction process applied to the seismograms to remove the *S*-wave anisotropy. (a) The radial (**R**) and transverse (**T**) components of a seismogram are successively rotated by 10° increments until the fast and slow *S* wave are clearly separated and aligned with the **R** and **T** directions, respectively. The rotation angle giving this alignment is the polarization angle of the fast *S* wave (ϕ). (b) The components are shifted by the delay time δt between the slow and fast *S* wave. (c) The seismogram components are submitted to an inverse rotation $-\phi$ to express them in the **R**–**T** coordinates.

For the other events, the noise level allowed no accurate determination of the parameters ϕ and δt to correct the seismograms.

4 FAULT PLANE SOLUTIONS

4.1 Methodology

Fault plane solutions are calculated following a non-linear inversion of the amplitudes of the direct *P*-, *Sv*- and *Sh*-waves (Godano *et al.* 2009). This method is suitable for the determination of focal mechanisms from sparse seismological networks. The *P, Sv* and *Sh* amplitudes are manually measured on the **L**, **R** and **T** filtered components of the rotated seismograms, respectively. The applied filter is a lowpass Butterworth at 300 Hz.

The direct problem of the method consists of modelling the far-field direct *P, Sv* and *Sh* theoretical amplitudes for a point-source in a flat layered medium, following the ray theory (Aki & Richards 1980). The modelling also includes the response of the sensors and the anelastic attenuation of the medium. The inverse problem is solved by a random exploration, derived from the Simulated Annealing Algorithm (Kirkpatrick *et al.* 1983). The parameter values explored by the algorithm are ϕ_f (the fault plane azimuth), δ (the fault plane dip) and λ (the fault plane rake). At each step of the exploration, the theoretical amplitudes corresponding to the explored parameters are compared to the observed amplitudes by computing a misfit function. The optimal solution corresponds to the parameters minimizing the misfit function. The exploration is divided in two steps: one enabling a wide exploration of the space parameters to localize the minima of the misfit function, and another exploring the minima of the misfit function to converge toward the absolute minimum. After obtaining the best solution, the scalar seismic moment M0 is determined as the ratio between the observed and the theoretical amplitudes corresponding to the optimal solution (ϕ_f^{opt}, δ^{opt} and λ^{opt}). The uncertainties of the focal mechanism are calculated by accounting for the convergence process of the inversion, the amplitude picking uncertainties caused by the noise level and the event location uncertainties. Uncertainties of the focal mechanism are computed by performing 100 inversions using random perturbed amplitudes and event locations. The results of these 100 inversions are called 'perturbed solutions'. The amplitudes are perturbed in increments following a Gaussian distribution with a standard deviation corresponding to that of a noise window immediately before the *P, Sv* and *Sh* amplitudes. The location is perturbed following Gaussian distributions with standard deviations equal to the uncertainties of the event coordinates. The standard deviations (σ_ϕ, σ_δ, σ_λ) of the distributions of the strike, dip and rake values corresponding to the 100 'perturbed solutions' give the uncertainty of the optimal solution. From these standard deviation values, a confidence interval is defined around the optimal solution:

$$I_c = \left[\phi_S^{\text{opt}} - \sigma_\phi, \phi_S^{\text{opt}} + \sigma_\phi\right] \bigcap \left[\delta^{\text{opt}} - \sigma_\delta, \delta^{\text{opt}} + \sigma_\delta\right] \bigcap \left[\lambda^{\text{opt}} - \sigma_\lambda, \lambda^{\text{opt}} + \sigma_\lambda\right] \quad (1)$$

The fault plane solution determination requires the use of Stations M0 and M1. The lack of information on the velocity model between the seismic swarm and M0 induces an uncertainty on the take-off angle at the source. This uncertainty is partially accounted for the perturbation of the event location during the computation of the focal mechanism uncertainties.

4.2 Resolution tests

We demonstrated (Godano *et al.* 2009) that a focal mechanism is correctly retrieved with a minimum of three 3-component stations. With two 3-component stations, as in the present station configuration, the accuracy of the focal solution depends on the station distribution in the focal sphere. Preliminary synthetic resolution tests are therefore performed to investigate how the fault plane solutions are constrained by the station configuration of the Arkema-Vauvert salt field.

We consider a $M_w = -2$ synthetic earthquake located in the area of the seismic swarm induced by the fluid injection at the PA22–PA23 wells doublet and recorded by Stations M0 and M1 (Fig. 9). The data (*P, Sv* and *Sh* amplitudes) are generated using the direct problem of the inversion method. The source time function duration of 0.0025 s is chosen in accordance with the observed data. The second column of Table 2 reports the parameters used for the modelling. The velocity model is derived from the velocity model of the Arkema-Vauvert field (Table 1), with identical layers. However, the *P* velocity are perturbed by $\pm$ 200 m s^{-1}, and the *S* velocity are obtained assuming a V_p/V_s ratio equal to 1,7. $Qp = Qs = 100$ is chosen with the range of values (99–150) found in salt rocks (Zimmer & Yaramanci 1993). The data are contaminated by a

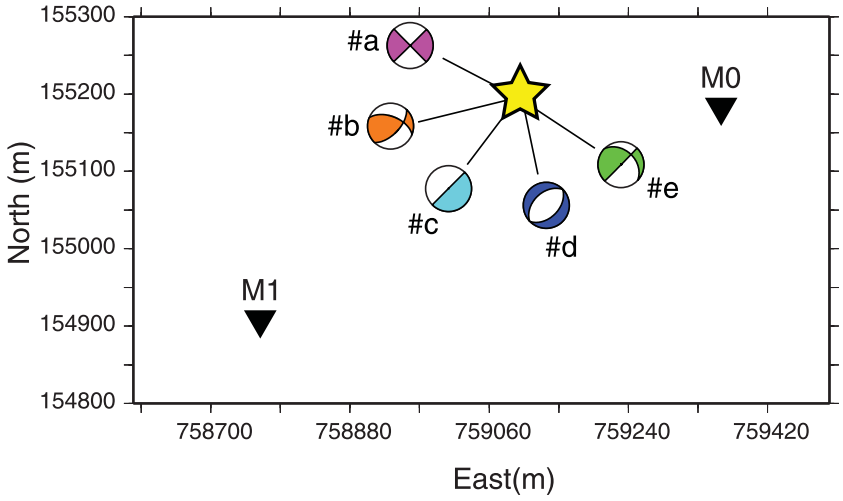

Figure 9. The earthquake location (yellow star) used for the two synthetic resolution tests. Black triangles indicate Stations M0 and M1. The beach balls indicate the focal mechanisms of the five synthetic events studied in the first test.

Table 2. Parameters used to compute the synthetic data and perform the inversion of the synthetic data.

Parameters		Synthetic Data Generation	Synthetic Data Inversion
Event easting coordinate (m)		759100	759150 ± 50
Event northing coordinate (m)		155200	155150 ± 50
Event depth coordinate (m)		2100	2050 ± 50
P- and *S*-wave velocity ($m\,s^{-1}$)	Layer #1	3500 and 2059	3700 and 2176
	Layer #2	4600 and 2706	4400 and 2588
	Layer #3	3800 and 2235	4000 and 2353
Q_P and Q_S		100 and 100	81 and 87

random white noise not exceeding 5 per cent of the maximum data amplitude.

The synthetic data are inverted using different parameter values (Table 2, third column) to reproduce real cases where event location, velocity model and anelastic attenuation are not perfectly known. The earthquake coordinates are perturbed by ±50 m in horizontal and vertical directions in agreement with the location uncertainties. The velocity model used for the inversion is the velocity model of the Arkema-Vauvert field. The difference in *P*-wave velocity between this model and the perturbed model used to generate data corresponds to an uncertainty in velocity of approximately 5 per cent. This value agrees with the one assumed in mining contexts (Silený & Milev 2006). The quality factors are those estimated by Godano *et al.* (2010) in the Arkema-Vauvert field.

We first perform a test consisting in the inversion of *P, Sv* and *Sh* amplitudes generated for five double–couple focal mechanisms with a fault plane striking 45° (Fig. 9). Table 3 presents the expected and retrieved fault plane solutions parameters, and Fig. 10 depicts the recovered focal mechanisms and related uncertainties. For each event, a stereodiagram displays the expected fault plane solution (blue), the recovered fault plane solution (red), the 'perturbed fault plane solutions' inside the confidence interval (eq. 1; black) and the 'perturbed fault plane solutions' outside the confidence interval (grey). These solutions are also plotted in a ternary diagram (e.g. Kagan 2005) enabling the analysis of a great number of focal mechanisms. The coordinates of each solution in the ternary diagram are obtained from the plunge angle of the *P-, T*- and null-axis. These coordinates are cartesian and range between −1 and 1 in *x* and *y* direction. We divide the diagram into seven areas delineated by lines corresponding to the 30° plunge of the *P*, *T* and null-axis. Area 1 corresponds to strike-slip faults, Area 2 to normal faults, Area 3 to thrust faults, Area 4 to normal-strike-slip faults, Area 5 to dip-slip faults, Area 6 to thrust-strike-slip faults and Area 7 to mixed faults. The star indicates the solution targeted for retrieval, the square indicates the recovered solution and the dots the 'perturbed solutions'.

Table 3. First resolution test: expected and recovered fault plane solutions given by the inversion of the synthetic data.

	Strike	Dip	Rake
Event #a			
Values to retrieve	45	90	0
Retrieved values	53	85	−14
Absolute difference	8	5	14
Uncertainties	35	8	8
Event #b			
Values to retrieve	45	60	40
Retrieved values	78	32	50
Absolute difference	33	28	10
Uncertainties	29	10	31
Event #c			
Values to retrieve	45	90	−90
Retrieved values	35	87	−68
Absolute difference	10	3	22
Uncertainties	56	11	46
Event #d			
Values to retrieve	45	45	−90
Retrieved values	59	44	−80
Absolute difference	14	1	10
Uncertainties	9	4	8
Event #e			
Values to retrieve	45	90	52
Retrieved values	45	84	53
Absolute difference	0	6	1
Uncertainties	24	8	33

The type of focal mechanism is correctly retrieved except for Event b. In this case, the expected and recovered solutions are not in the same area of the ternary diagram. The recovered solution displays a more important inverse component than the expected solution. The 'perturbed solutions' are very sparse and spread over several areas of the ternary diagram. The azimuths of the nodal planes are correctly retrieved with a difference between the expected and recovered solutions ranging from 0° to 15° (Table 3), except for Event b, which featured a difference greater than 30°. The estimated strike, dip and rake uncertainties are globally equal to or greater than the difference between the expected and recovered parameters. The uncertainties are significantly underestimated, comparing to the difference between the expected and recovered solutions for the azimuth of Event d, the dip of Event b and the rake of Event a.

We undertake a second test with numerous focal mechanisms characterized by various azimuths. Data are generated for 1056 synthetic focal mechanisms plotted in the ternary diagram of Fig. 11(a). Each point corresponds to eight focal mechanisms with a similar dip and rake and with an azimuth ranging between 0° and 315°, varying by a step of 45°. The data are symmetrically distributed along the median of the triangle. The left part of the triangle corresponds to the data with a negative rake, and the right part corresponds to the data with a positive rake.

Fig. 11(b) depicts the results of the synthetic data inversion. The type of focal mechanism is correctly retrieved for 74 per cent of the solutions. Table 4 reports the detailed percentages of the correctly recovered solution for each type of focal mechanism. The best recovered solutions are the strike-slip (91 per cent) and dip-slip (83 per cent) fault plane solutions. The mixed fault plane solutions (Area 7) are retrieved poorly (29 per cent), due to the reduced surface of Area 7 versus the other area. Numerous solutions thus fall in the neighbour areas.

The distributions of the strike, dip and rake uncertainties for the 1,056 solutions are given in Fig. 11 for each area of the ternary diagram. Table 4 provides the minimal, maximal and median value

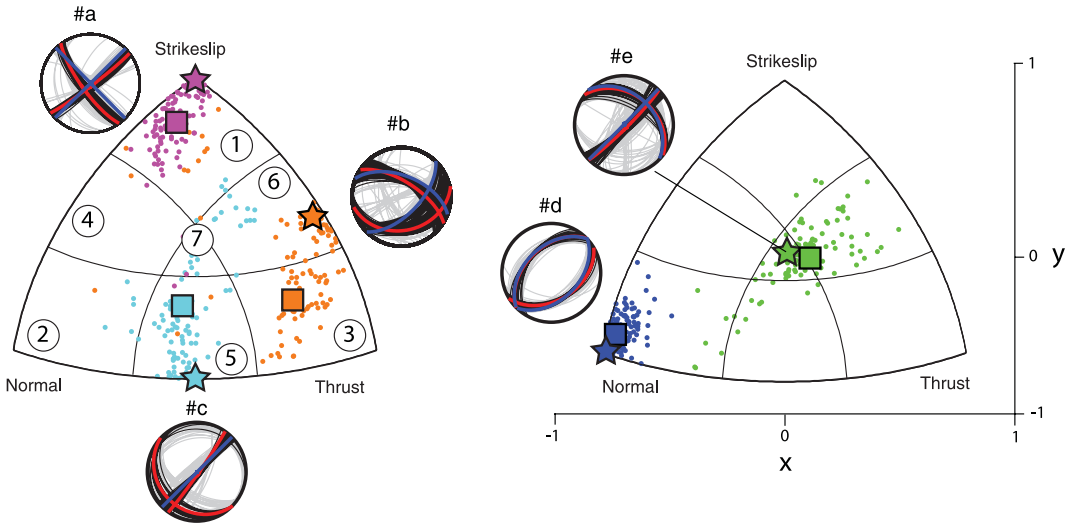

Figure 10. The results of the first synthetic resolution test. For each event, the stereodiagram displays the expected fault plane solution (blue), the recovered fault plane solution (red), the 'perturbed fault plane solutions' inside the confidence interval (eq. 1) (black) and the 'perturbed fault plane solutions' outside the confidence interval (grey). The ternary diagrams display for each event the solution to retrieve (star), the recovered solution (square) and the 'perturbed solutions' (dot). Each corner of the triangle corresponds to the vertical null-axis (strike-slip fault), *P*-axis (normal fault) and *T*-axis (thrust fault). The line inside the ternary diagram indicates the 30° plunge angle of the null-, *P*- and *T*-axis and delineates seven areas corresponding to a type of focal mechanism: strike-slip fault (Area 1), normal fault (Area 2), inverse fault (Area 3), normal-strike-slip fault (Area 4), dip-slip fault (Area 5), thrust-strike-slip fault (Area 6) and mixed fault (Area 7).

for each distribution. The dip uncertainties range between 0° and 20° regardless of the type of focal mechanism. The median is approximately 5–10°. The median of the strike uncertainties is approximately 15–17° for Areas 2, 3, 4 and 6 and is greater for the other areas (from 34° to 45°). The median of the rake uncertainties scales around 15–20° for Areas 1, 2, 3, 4 and 6 and is greater (45° and 34°) for Areas 5 and 7.

The second test highlights that the station configuration in the Arkema-Vauvert salt field enables the determination of the focal mechanism type for nearly 75 per cent of the synthetic earthquakes. The strike-slip and dip-slip focal mechanisms are better retrieved than the other solutions but their strike uncertainty is great. Identically, the rake uncertainty is great for the dip-slip solutions. The dip is the best retrieved parameter independently of the type of focal mechanism. All these differences are the consequence of the station geometry with respect to the event location.

4.3 Real data results

The focal mechanisms are computed for the 638 anisotropy-corrected earthquakes. The uncertainties describe the stability of these focal mechanisms. Fig. 12 displays examples of the unconstrained focal mechanisms for four seismic events. We consider a focal solution unconstrained if there are two distinct and equivalent families of perturbed solutions (Fig. 12a), if the perturbed solution are scattered (Fig. 12c) and/or if the *P* and *T* axis of the perturbed solutions are not clustered (Figs 12b and 12d). A visual analysis of the uncertainties discards seismic events with unconstrained focal mechanism. Finally, we retain 532 constrained focal mechanisms.

Fig. 13(a) illustrates seven examples of the 532 focal mechanisms. The beach ball and the uncertainties of the seven fault plane solutions are also displayed. The focal solutions are relatively well constrained. The plot of the waveform at Stations M0 and M1 in Fig. 13(b) corroborates these results and depicts a good fit between the observed and the computed amplitudes.

The uncertainties of 532 focal mechanisms are displayed in the histograms of Fig. 14. The median uncertainties on the strike, the dip and the rake equal 27.8°, 7.4° and 26.5°, respectively. The dip is better retrieved than the strike and rake. This is in accordance with the results of the synthetic tests.

The 532 constrained focal mechanisms are displayed in Figs 15(a), 16(a) and 17(a) for each period highlighted in Section 3.1. The solutions are plotted in the top ternary diagram. The nodal plane and the *P* and *T* axes are also plotted for all focal mechanisms of each area of the diagram. The corresponding confidence domain is represented by the density plot of the 'perturbed solutions' in the bottom-left ternary diagram. The density plot is obtained by considering a grid with a step of 0.05 along the *x* and *y* direction in the cartesian coordinate system. The number of perturbed solutions is counted at each node of the grid. Next, a bicubic interpolation is used to smooth the image. The rose diagram presents the azimuth uncertainties and displays the nodal-planes azimuth distribution of the perturbed solutions. These figures illustrate that the majority of the earthquakes have fault plane solutions between thrust fault and dip-slip fault type (Areas 3, 5, 6 and 7). Moreover, the majority of the focal mechanisms have nodal planes with similar orientations (NE–SW and N–S to NW–SE). This indicates that the seismic ruptures occur primarily on one fault family corresponding to one of the nodal planes. The solutions of Areas 5 and 7 display *P* and *T* axis evenly divided into two families, one in accordance with the thrust fault solutions and the other with normal fault solutions.

Period 1(Fig. 15a) is characterized by a majority of thrust-strike-slip faults earthquakes (area 6 of the ternary diagram) with N–S and NE–SW nodal planes. The synthetic tests (Fig. 11) indicate such focal mechanisms are reasonably well constrained by the station geometry. Period 1 also displays a significant number of dip-slip fault earthquakes (area 5 of the ternary diagram) that are less well

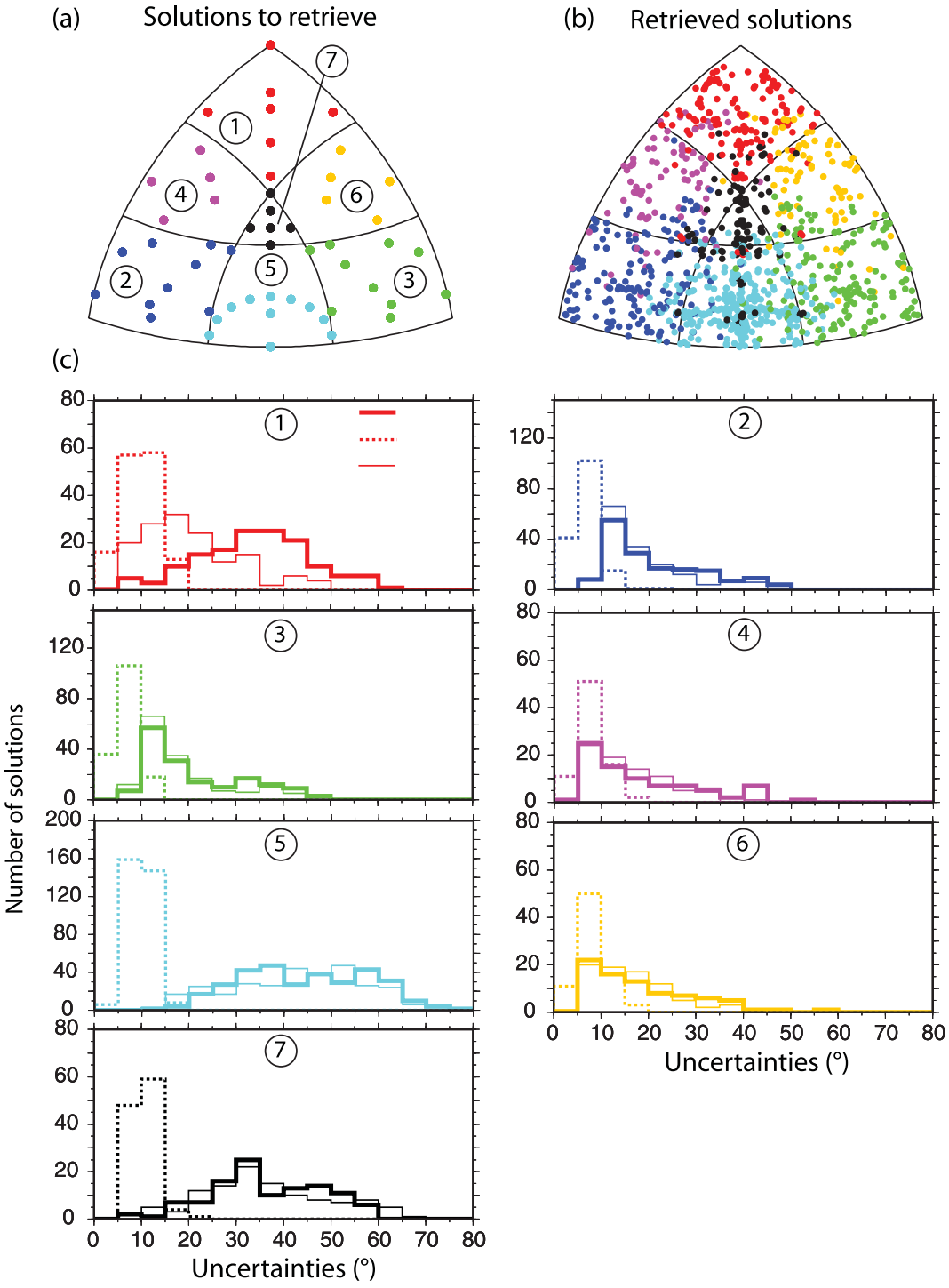

Figure 11. The results of the second synthetic resolution test. (a) Ternary diagram displaying the 1056 focal mechanisms to retrieve. Each dot corresponds to eight focal mechanisms with azimuth ranging between 0° and 315°. (b) Ternary diagram of the recovered solutions. (c) Histograms of the strike, dip and rake uncertainties of the recovered fault plane solutions.

constrained in azimuth and rake than thrust-strike-slip solutions, as highlighted in the synthetic tests. The ternary diagram of the confidence domain (Fig. 15a) also displays high 'perturbed solutions' density in the areas 6 and 5. The rose diagram indicates an uncertainty of approximately 30° for the NE–SW nodal plane and approximately 60° for the N–S nodal plane.

Period 2 (Fig. 16a) is dominated by thrust-fault earthquakes with different orientations, and some dip-slip and strike-slip-inverse fault earthquakes occur with NE–SW and NS to NW–SE nodal planes. Synthetic tests show that thrust-fault earthquakes are well recovered (Fig. 11). The confidence domain is characterized by several high 'perturbed solution' density zones. In fact, these zones result from the low number of events in Period 2 and do not indicate solution variability. Identically, the rose diagram indicates several sparse nodal plane directions (NE–SW, N–S, E–W and NW–SE) due to the low number of events.

Table 4. Second resolution test: Percentages of the correctly retrieved solutions for each type of focal mechanism. Minimal, median and maximal values of the distributions of the strike, dip and rake uncertainties for each type of focal mechanism.

Ternary diagram area	Correctly retrieved solution type (per cent)	Strike uncertainty (°)			Dip uncertainty (°)			Rake uncertainty (°)		
		min	median	max	min	median	max	min	median	max
#1	91	6	34	64	3	10	20	4	19	49
#2	75	8	17	49	2	6	20	7	15	58
#3	75	8	17	48	2	6	13	7	16	50
#4	73	2	15	54	3	7	18	6	14	43
#5	83	14	45	73	3	10	18	11	45	102
#6	73	5	15	56	3	8	19	5	15	42
#7	29	6	34	59	5	10	22	9	34	66

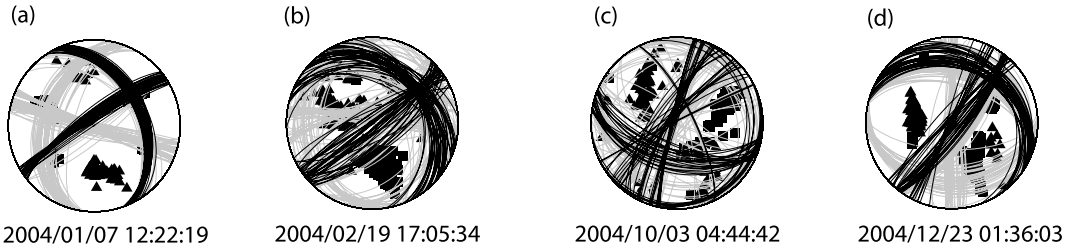

Figure 12. Examples of uncertainty diagrams for four unconstrained focal mechanisms. Black: perturbed solution inside the confidence interval (see text for details). Grey: perturbed solution outside the confidence interval. *P* (triangle) and *T* (square) axis of each perturbed solution are also displayed.

Period 3 (Fig. 17a) is dominated by thrust dip-slip fault earthquakes (Areas 3, 5, 6 and 7 of the ternary diagram) with NE–SW and NW–SE nodal planes. Numerous normal to normal-strike-slip fault solutions with NW–SE and NS to NW–SE nodal planes and some strike-slip fault solutions with N–S and E–W nodal planes also occur. These results are corroborated by the confidence domain density plot. The rose diagram indicates an uncertainty of approximately 15° for the NE–SW nodal plane and approximately 45° for the NW–SE nodal plane. The synthetic tests (Fig. 11) indicate a good recovering of normal and normal-strike-slip fault earthquakes but great uncertainties on strike for strike-slip fault and on strike and rake for dip-slip fault earthquakes.

Correlations between the focal mechanisms and the spatio-temporal distribution of the seismic activity are highlighted in Figs 15(b), 16(b) and 17(a). During Period 1, the deep earthquakes located in the lower allochthonous series are thrust-strike-slip faults. The shallow earthquakes located near the D2 fault plane are dip-slip. Period 2 corresponds with the minor seismic crisis following the second inversion of the injector well and is characterized by a majority of thrust-fault earthquakes located at the depth of the D2 fault plane. Period 3 corresponds to the major seismic crisis and is characterized by:

(1) some normal to normal-strike-slip events at the base of the seismic swarm (lower allochthonous series),

(2) numerous thrust to dip-slip events at the depth of the D2 fault plane, and

(3) some strike-slip events at the top of the seismic swarm (upper allochthonous series).

5 DISCUSSION

The focal mechanisms are determined assuming shear faulting (double–couple). The two 3-component station configuration in the Arkema-Vauvert salt field prevents the determination of the general moment tensor and the investigation of non-double–couple components in the seismic rupture. If the double–couple rupture process is valid, then the majority of studied earthquakes may be dip-slip to thrust faults occurring on NE–SW subvertical structure or on N–S to NW–SE subhorizontal structures. On the other hand, if a dominant non-double–couple component occurs in the rupture process, the computed fault plane solutions cannot be interpreted. Jechumtálová & Šilený (2005) illustrates that the inverting data of a non-double–couple event can provide distorted fault plane solution by imposing a double–couple constraint. Regardless of the hypothesis on the source rupture process, focal mechanisms variations occur and are correlated with the three periods of seismic activity.

Several observations indicate that shear faulting is dominant in the Arkema-Vauvert salt field. As explained in Section 2.1, water circulating through the network of fractures between two wells dissolves the salt. Over the long term, the water circulation creates two vertical cavities along the wells, but the seismicity is globally located between these cavities. This indicates that the earthquakes are primarily induced by water circulation through fractures as in hydro-fracturing experiments. Dahm *et al.* (1999) already depicted that the microearthquakes induced by hydro-fracturing in salt rock (Bernburg Mine, Germany) display a major double–couple component.

Comparisons between the Arkema-Vauvert salt field and the Cerville-Buissoncourt salt field (Mercerat *et al.* 2010) depict strong differences in the induced seismic events. In the Cerville-Buissoncourt site, water injections create one brine-filled cavern at 200 m depth in a salt series. Two types of seismic events are recorded:

(1) Few isolated microearthquakes located in the cavern surroundings within the salt layer and the intercalated marls. For these events, the presence of extensive components in the source mechanisms is suggested by the ratio between the displacement spectra of the *S* (Ω_0^S) and *P* (Ω_0^P) waves lower than 4 (Walter & Brune 1993).

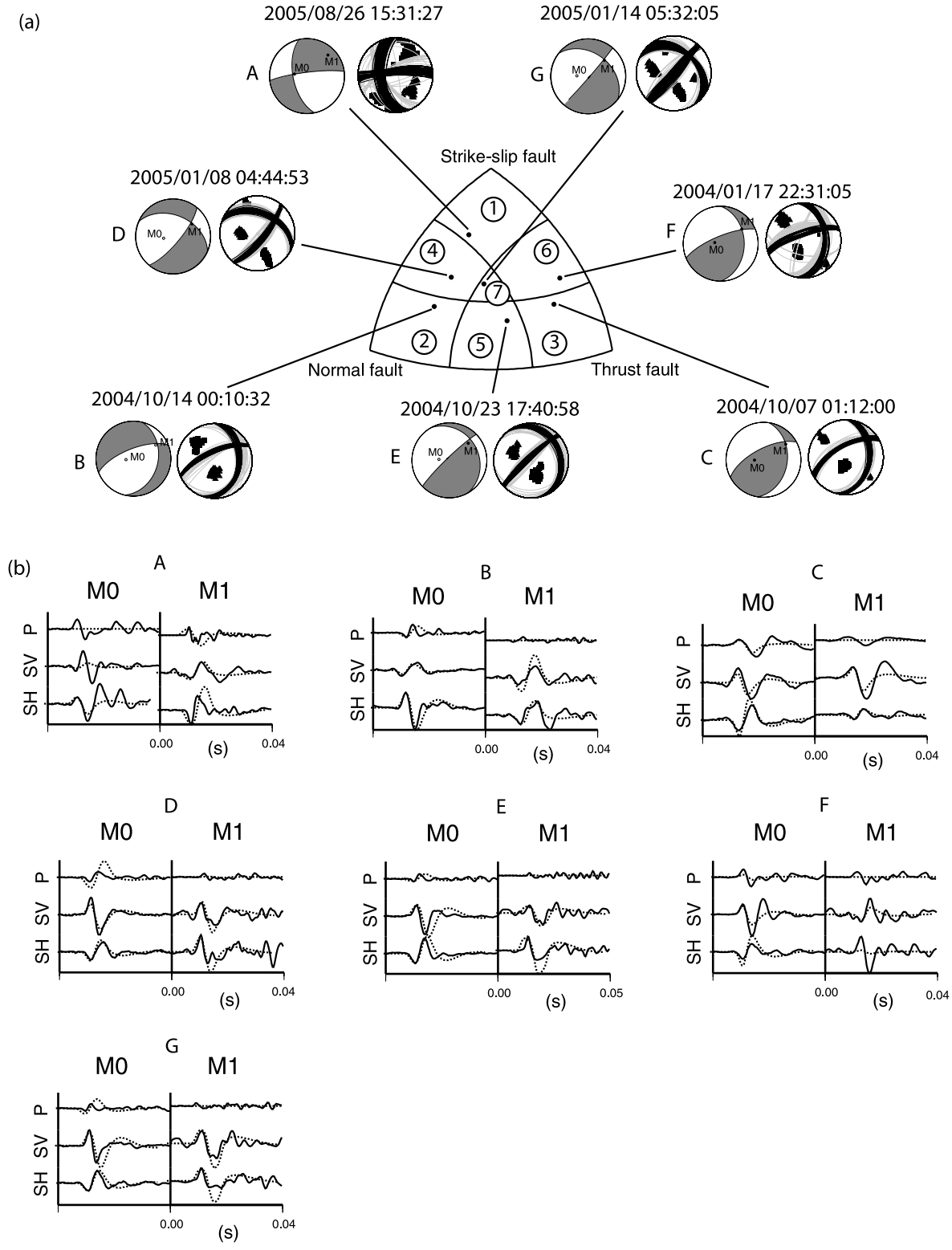

Figure 13. (a) Examples of constrained focal mechanisms displayed in a ternary diagram and associated uncertainties. The symbols are the same as in Fig. 12. (b) Observed (solid line) and computed seismograms (dotted line). The traces are scaled with respect to each station.

(2) A substantial majority of tremor-type events with 10 seconds of duration. The authors suggest that these tremor-type events are the consequence of large block falls and debris flows within the brine-filled cavern.

In the Arkema-Vauvert salt field, we identified no tremor-type events. Thus, block falls and debris flow in the cavities did not likely cause the seismicity. Table 5 provides the values of (Ω_0^P) and (Ω_0^S) (Godano *et al.* 2010) for 15 events recorded during the

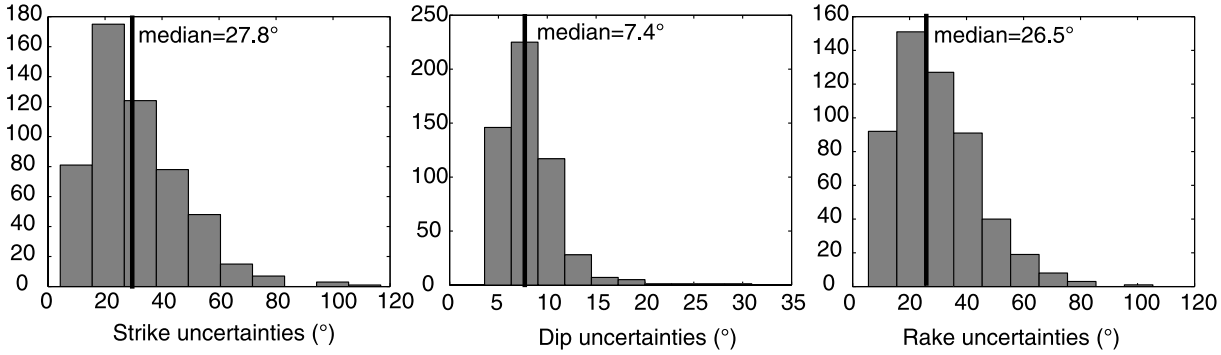

Figure 14. Histogram of the uncertainties on the strike, dip and rake for the 532 computed focal mechanisms.

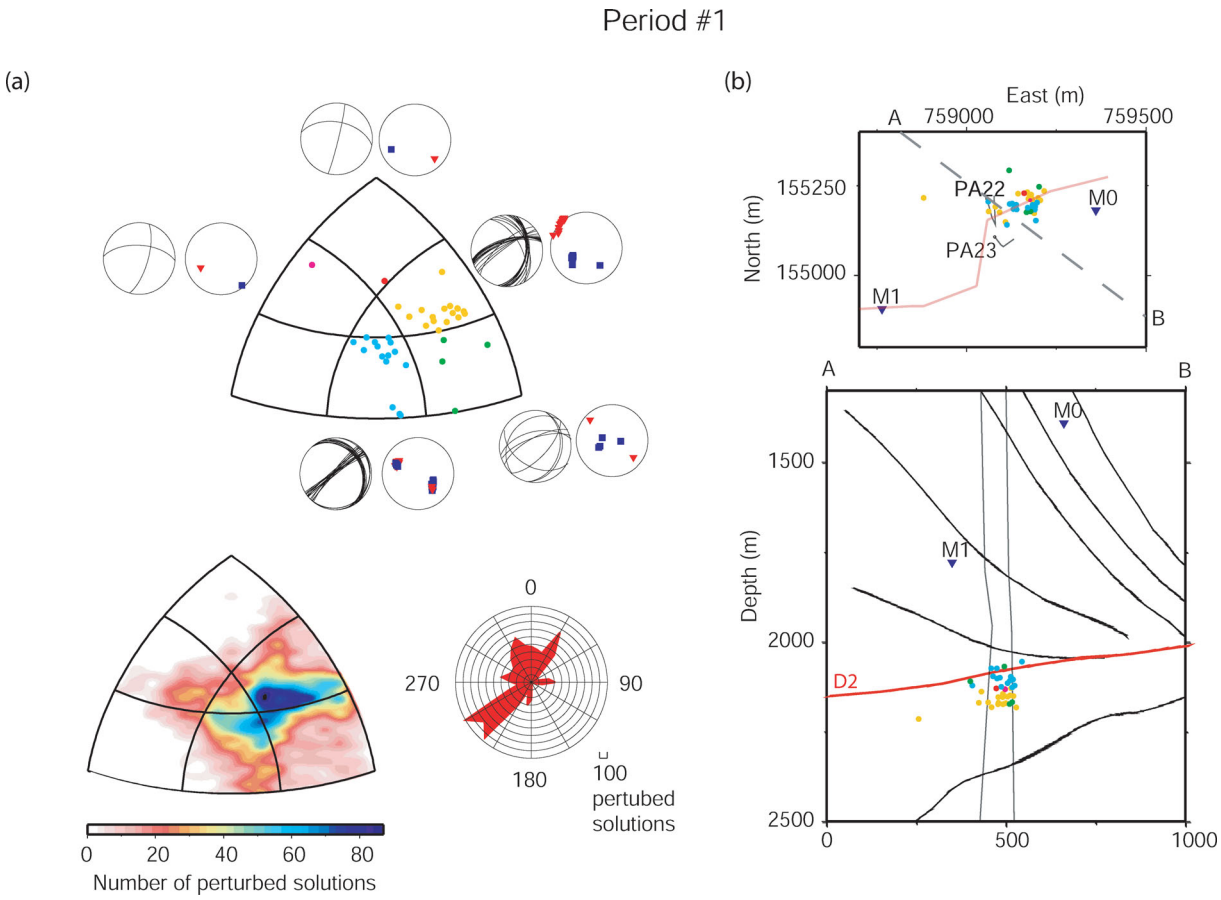

Figure 15. Focal mechanisms of earthquakes induced during Period 1. (a) Ternary diagram and stereodiagrams displaying the fault plane solution and the *P* (red triangle) and *T* (blue square) axis (top panel); density plot of the 'perturbed solutions' displaying the confidence domain of the focal mechanisms (bottom-left panel) and rose diagram of the 'perturbed solutions' azimuth displaying the azimuth confidence domain of the focal mechanisms (bottom-right panel). The number in the lower right corner of the rose diagram indicates the radial step of the grid. (b) Map and cross-section of the seismicity induced during Period 1. The colour indicates the type of focal mechanism: strike-slip fault (red), normal fault (blue), inverse fault (green), normal-strike-slip fault (magenta), dip-slip fault (cyan), thrust-strike-slip fault (orange) and mixed fault (black).

field deployment of a temporary antenna in 2008 March. The ratio Ω_0^S/Ω_0^P ranges globally between 4 and 7, indicating a predominance of the shear component in the source rupture mechanism ($\Omega_0^S/\Omega_0^P \sim 7.1$ for pure shear fault).

Several limitations prevent the proposition of a geological model explaining the computed focal mechanisms. The location of the seismicity is obtained from only one of the two permanent 3-component seismological sensors (M1). The velocity model used for the locations is also relatively simple in the context of the geologic complexity of the field. These two problems induce non-negligible uncertainties in the earthquake locations. On the other hand, the focal mechanisms are determined from the two permanent 3-component stations. As for the locations, the uncertainties of the focal mechanisms are non-negligible. The contribution of these uncertainties only allows for an estimation of the seismological process in the field.

Despite these uncertainties, we investigate which geological structures in the reservoir can be responsible of the observed seismicity. At the depth of the seismicity two types of geological structures can be identified (Fig. 18):

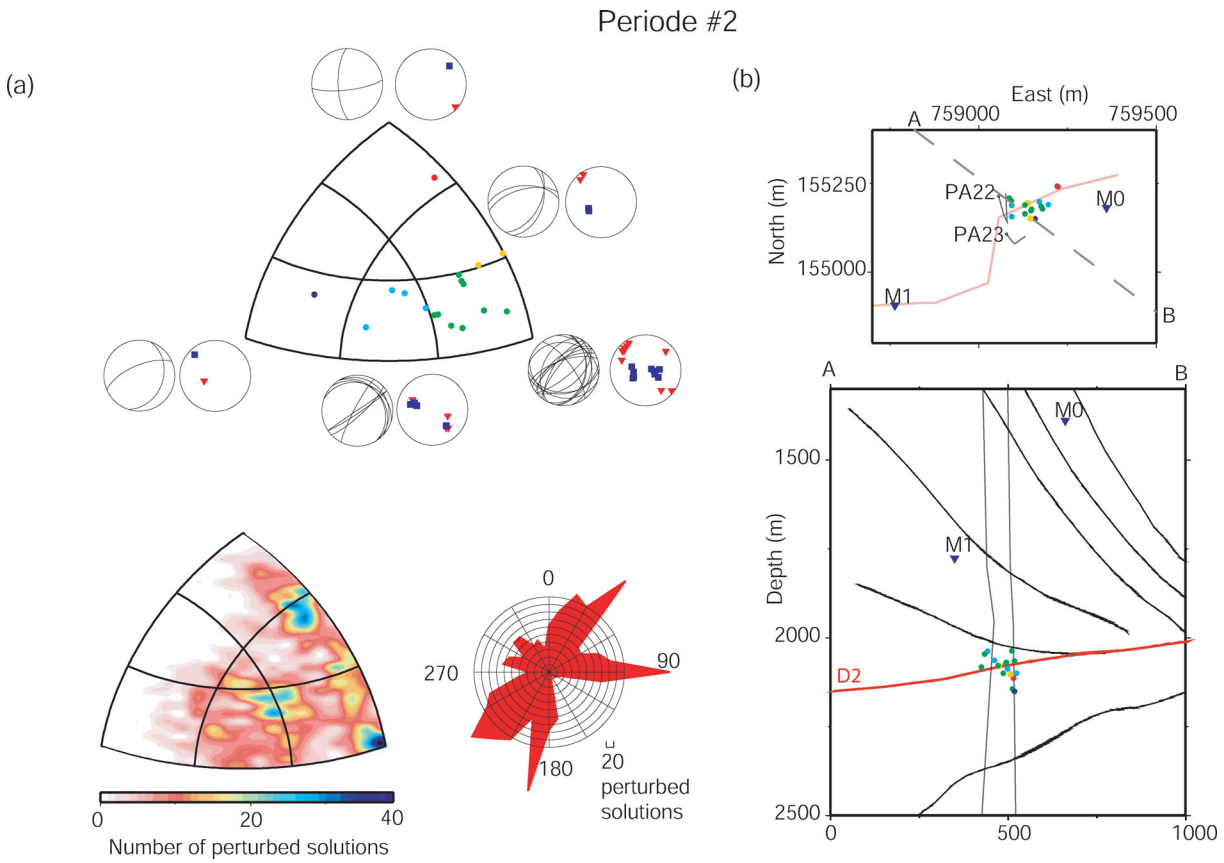

Figure 16. Same as Fig. 15 but for the period #2.

(1) the subhorizontal D2 thrust fault striking NE–SW, and
(2) the stratigraphic interfaces (S) between the beds of salt and the beds of insoluble rocks in the upper and lower allochthonous salt series (NE–SW, subvertical near D2).

The majority of the determined focal mechanisms (dip-slip and thrust fault) display a NE–SW subvertical nodal plane (P1) and a N–S to NW–SE subhorizontal nodal plane (P2) (Fig. 18).

The dip of P2 is incompatible with the dip of D2 and the azimuth of P1 is incompatible with the azimuth of D2. As seen in Section 4.2, the synthetic tests give a median dip uncertainty around 10° for the dip-slip solutions. This low uncertainty cannot explain the great difference between the dip of P2 and the dip of D2. On the other hand, the median strike uncertainty is around 45° for the dip-slip solutions and could explain the azimuthally difference between D2 and P1. Thus the nodal plane P1 could correspond to the D2 fault. This hypothesis is in accordance with the seismicity observed around the D2 fault, but does not explain the seismicity observed in the lower allochthonous salt series.

Another hypothesis is the seismicity might occur along the stratigraphic planes (S). As displayed in Fig. 18, *S* is in accordance (in azimuth and dip) with P2. This hypothesis could explain the observed seismicity in the lower allochthonous salt series and around the fault D2.

This study shows that the instrumentation of a minimalistic monitoring network for underground operations (Enhanced geothermal system, gas and oil production, brine production or other mining activity) can be optimized in advance. Taking into account the expected rupture mechanisms given by geological information, synthetic tests can be performed to investigate how well the expected focal mechanisms are retrieved with minimalistic station geometries. Nevertheless, the configuration of the current permanent seismological network in the Arkema-Vauvert salt field is not optimal for a detailed investigation of all processes related to water injection. The deployment of some additional seismological station may improve the characterization of the velocity model, the location of the seismicity using relative location methods as the double-difference (Waldhauser & Ellsworth 2000) and the multiplets analysis. Additional stations may also improve the precision of fault plane solutions and the determination of the moment tensor to investigate possible non-double–couple rupture processes (e.g. Dziewonski *et al.* 1981; Godano *et al.* 2011).

6 CONCLUSION

In this paper, we depicted the type of information provided by the microseismicity recorded with a minimalist seismological network and the limitations to a detailed understanding of the fracturing process in the reservoir. We studied a microseismic swarm induced by injection operations in the Arkema-Vauvert salt-field (Wells PA22 and PA23). The seismic activity in this field is monitored by two permanent 3-component stations deployed in two wells. The study focused on a period of 21 months between 2004 January and 2005 September.

Using Station M1, 1214 seismic events were located, highlighting three main periods that correlated with the water-injection operations. They indicated a migration of the seismicity toward the D2 thrust fault and a hydraulic connection between Wells PA22 and PA23.

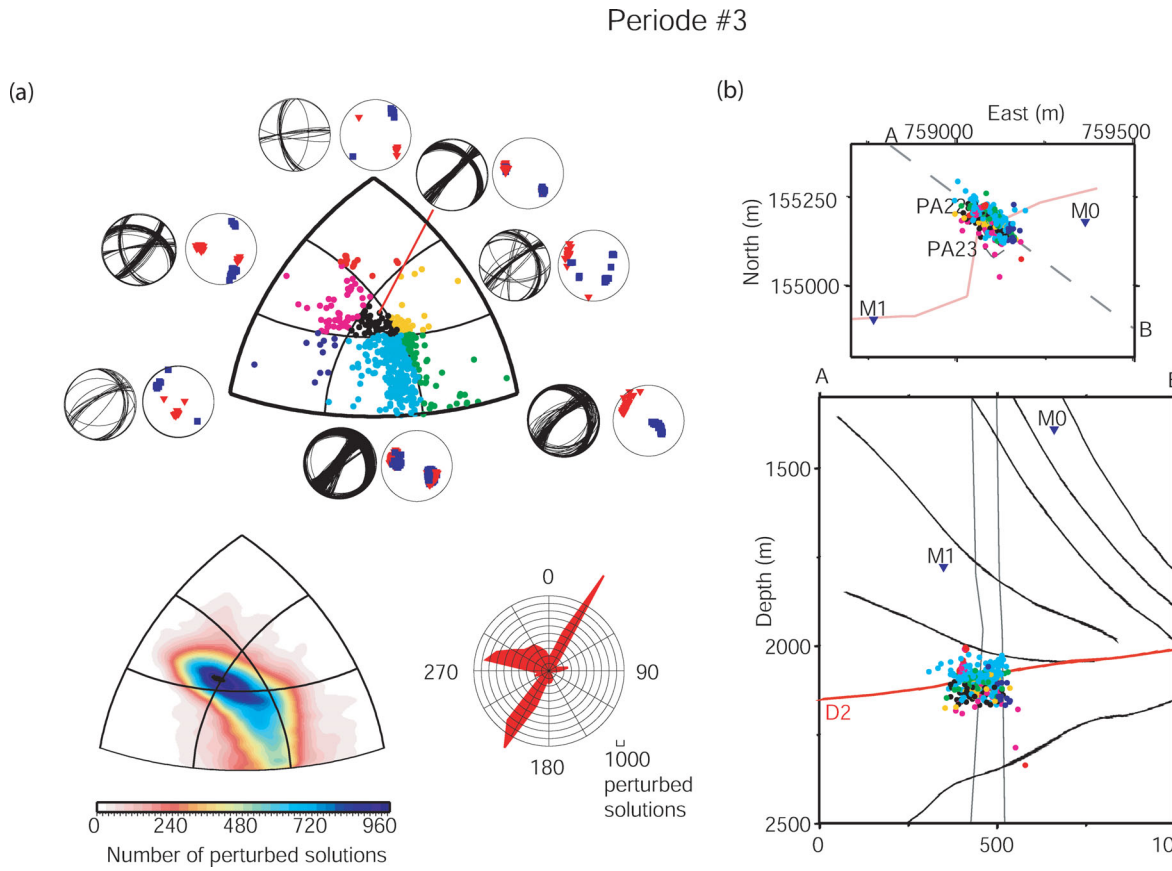

Figure 17. Same as Fig. 16 but for the period #3.

Table 5. Displacement spectra of the P (Ω_0^P) and S (Ω_0^S) waves for 15 earthquakes induced in the Arkema-Vauvert salt field in 2008 (Godano *et al.* 2010) and the corresponding Ω_0^S/Ω_0^P ratio.

Event	Ω_0^P (10^{-11} m s^{-1})	Ω_0^S (10^{-11} m s^{-1})	Ω_0^S/Ω_0^P
#1	0.95	4.03	4.24
#2	0.64	4.10	6.40
#3	-	5.66	-
#4	7.27	93.70	12.88
#5	0.81	3.77	4.65
#6	0.46	3.47	7.54
#7	-	3.35	-
#8	2.86	8.93	3.12
#9	0.45	2.68	5.95
#10	2.32	10.03	4.32
#11	7.37	39.31	5.33
#12	0.44	1.98	4.5
#13	-	6.68	-
#14	1.08	8.05	7.45
#15	1.23	7.22	5.87

A waveform analysis revealed S-wave anisotropy that is problematic for determining the focal mechanisms from the direct-wave amplitudes. Therefore, the seismograms were corrected by removing the anisotropy.

Focal mechanisms were computed using *P, Sv* and *Sh* amplitudes manually measured on anisotropy-corrected seismograms. Synthetic resolution tests were performed to assess the reliability of the focal mechanism determination from the two 3-component stations deployed in the field. Synthetic data were generated for 1056 earthquakes with various focal mechanisms. The results indicate that the type of focal mechanism is correctly retrieved for 74 per cent of the synthetic earthquakes, but the uncertainties of the strike and rake are significant (from 15° to 45°). The focal mechanisms

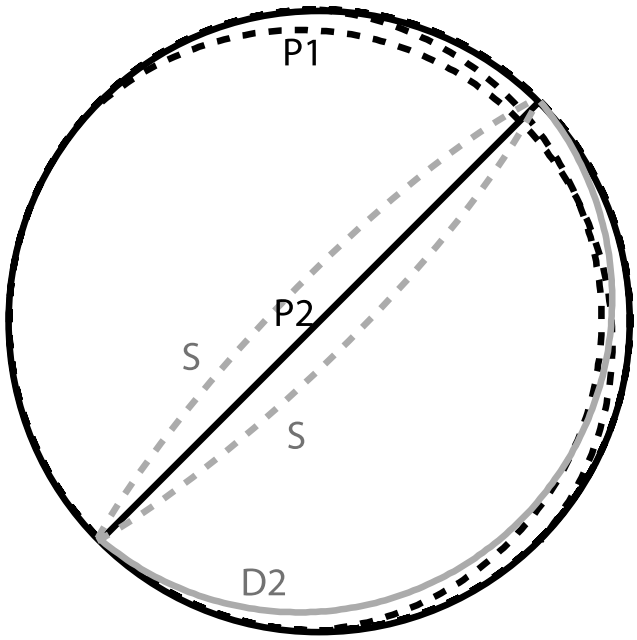

Figure 18. Stereographic diagram displaying the D2 thrust fault, the stratigraphic plane S and the nodal plane P1 and P2 of the dip-slip and thrust fault focal mechanisms.

were computed for 532 real earthquakes. The solutions correspond primarily to a dip-slip fault type with subhorizontal NE–SW and subvertical N–S nodal planes. Correlations between the focal mechanisms and the spatio-temporal distribution of the seismic activity were highlighted.

This study showed it is possible to reliably retrieve double–couple focal mechanisms for some faulting geometries with a minimalistic 2-stations network. However, the reliability of the focal mechanism retrieval depends on the station configuration. Therefore, the addition of further stations surely improves the results obtained in this study.

DATA AND RESOURCES

The figures presented in this paper were generated by Generic Mapping Tools (GMT).

ACKNOWLEDGMENTS

This work has been supported by the Magnitude Society. We gratefully acknowledge comments by two anonymous reviewers who helped to improve the initial manuscript.

REFERENCES

Aki, K. & Richards, P., 1980. *Quantitative Seismology: Theory and Methods,* W. H. Freeman and Co., San Francisco, CA.

Ando, M., Ishikawa, Y. & Yamazaki, F., 1983. Shear wave polarization anisotropy in the upper mantle beneath Honshu, Japan, *J. geophys. Res.,* **88**(B7), 5850–5864.

Aster, R., Shearer, P. & Berger, J., 1990. Quantitative measurements of shear wave polarizations at the Anza seismic network, southern California: implications for shear wave splitting and earthquakes prediction, *J. geophys. Res.,* **95**(B8), 12 449–12 473.

Bohnhoff, M., Dresen, G., Ellsworth, W.L. & Ito, H., 2010. Passive seismic monitoring of natural and induced earthquakes: case studies, future directions and socio-economic relevance, in *New Frontiers in Integrated Solid Earth Sciences*, *International Year of Planet Earth,* pp. 261–285, eds Mulder, E.F., Derbyshire, E., Cloetingh, S. & Negendank, J., Springer, Dordrecht.

Dahm, T., Manthei, G. & Eisenblatter, J., 1999. Automated moment tensor inversion to estimate source mechanisms of hydraulically induced microseismicity in salt rock, *Tectonophysics,* **306,** 1–17.

Delouis, B. & Legrand, D., 1999. Focal mechanism determination and identification of the fault plane of earthquakes using only one or two near-source seismic recordings, *Bull. seism. Soc. Am.,* **89**(6), 1558–1574.

Dziewonski, A., Chou, T.-A. & Woodhouse, J., 1981. Determination of earthquake source parameters from wave-form data for studies of global and regional seismicity, *J. geophys. Res.,* **86,** 2825–2852.

Elkibbi, E. & Rial, J., 2005. The Geysers geothermal field: results from shear-wave splitting analysis in a fractured reservoir, *Geophys. J. Int.,* **162,** 1024–1035.

Godano, M., Regnier, M., Deschamps, A., Bardainne, T. & Gaucher, E., 2009. Focal mechanisms from sparse observations by nonlinear inversion of amplitudes: method and tests on synthetic and real data, *Bull. seism. Soc. Am.,* **99**(4), 2243–2264.

Godano, M., Gaucher, E., Bardainne, T., Regnier, M., Deschamps, A. & Valette, M., 2010. Assessment of focal mechanisms of microseismic events computed from two three-component receivers: application to the arkema-vauvert field (France), *Geophys. Prospect.,* **58,** 775–790.

Godano, M., Bardainne, T., Regnier, M. & Deschamps, A., 2011. Moment tensor determination by nonlinear inversion of amplitudes, *Bull. seism. Soc. Am.,* **101**(1), 366–378.

Hardebeck, J. & Shearer, P., 2002. A new method for determining first-motion focal mechanisms, *Bull. seism. Soc. Am.,* **92**(6), 2264–2276.

Hardebeck, J. & Shearer, P., 2003. Using S/P amplitude ratios to constrain focal mechanisms of small earthquakes, *Bull. seism. Soc. Am.,* **93**(6), 2434–2444.

Jechumtálová, Z. & Šilený, J., 2005. Amplitude ratios for complete moment tensor retrieval, *Geophys. Res. Lett.,* **32,** L22303, doi:10.1029/2005GL023967.

Kagan, Y., 2005. Double-couple earthquake focal mechanism: random rotation and display, *Geophys. J. Int.,* **163,** 1065–1072.

Kirkpatrick, S., Gelatt, C. & Vecchi, M., 1983. Optimization by simulated annealing, *Science,* **220**(4598), 671–680.

Langston, C., 1982. Single-station fault plane solutions, *Bull. seism. Soc. Am.,* **72**(3), 729–744.

Maisons, C., Fortier, E. & Valette, M., 1997. Induced microseismicity and procedure for closure of brine production caverns, *Pure appl. Geophys.,* **150,** 585–603.

Maxwell, S. & Urbancic, T., 2005. The potential role of passive seismic monitoring for real-4D reservoir characterization, *SPE Reser. Eval. Eng.,* **8**(1), 70–76.

Mercerat, E., Driad-Lebeau, L. & Bernard, P., 2010. Induced seismicity monitoring of an underground salt cavern prone to collapse, *Pure appl. Geophys.,* **167,** 5–25.

Phillips, W., Rutledge, J., House, L. & Fehler, M., 2002. Induced microearthquake patterns in hydrocarbon and geothermal reservoirs: six case studies, *Pure appl. Geophys.,* **159,** 345–369.

Raucoules, D., Maisons, C., Carnec, C., Mouelic, S.L., King, C. & Hosford, S., 2003. Monitoring of slow ground deformation by ERS radar interferometry on the Vauvert salt mine (France). Comparison with ground-based measurement, *Remote Sens. Environ.,* **88,** 468–478.

Reasenberg, P. & Oppenheimer, D., 1985. FPFIT FPPLOT and FPPAGE: FORTRAN computer programs for calculating and displaying earthquake fault-plane solutions, *U.S. Geol. Surv. Open File Rep.,* pp. 85–739.

Séranne, M., Benedicto, A. & Labaum, P., 1995. Structural style and evolution of the Gulf of Lion Oligo-Miocene rifting: role of the Pyrenean orogeny, *Mar. Petrol. Geol.,* **12**(8), 809–820.

Silený, J. & Milev, A., 2006. Seismic moment tensor resolution on a local scale: simulated rockburst and mine induced seismic events in the Kopanang gold mine, South Africa, *Pure appl. geophys.,* **163,** 1495–1513.

Silený, J. & Milev, A., 2008. Source mechanism of mining induced sesimic events—resolution of double couple and non double couple models, *Tectonophysics,* **456,** 3–15.

Sipkin, S., 1987. Moment tensor solutions estimated using optimal filter theory, *Phys. Earth planet. Inter.,* **47,** 67–79.

Snoke, J., 2003. *FOCMEC: FOCal MEChanism determinations, in Internationnal Handbook of Earthquake and Engineering Seismology,* Elsevier, New York, NY.

Stump, B. & Johnson, L., 1977. The determination of source properties by the linear inversion of seismograms, *Bull. seism. Soc. Am.,* **67,** 1489–1502.

Tang, C., Rial, J. & Lees, J., 2008. Seismic imaging of geothermal field at Krafla, Iceland using shear-wave splitting, *J. Volc. Geotherm. Res.,* **176,** 315–324.

Valette, M. & Benedicto, A., 1995. Chevauchements gravitaires halotectoniques dans le bassin distensif de Camargue (marge du golfe du Lion, SE de la France), *Bull. Soc. geol. France,* **166**(2), 137–147.

Vlahovic, G., Elkibbi, M. & Rial, J., 2002. Shear-wave splitting and reservoir crack characterization: the Coso geothermal field, *J. Volc. Geotherm. Res.,* **120,** 123–140.

Waldhauser, F. & Ellsworth, W., 2000. A double-difference earthquake location algorithm: method and application to the Northern Hayward fault, California, *Bull. seism. Soc. Am.,* **90**(6), 1353–1368.

Walter, W. & Brune, J., 1993. Spectra of seismic radiation from a tensile crack, *J. geophys. Res.,* **98,** 4449–4459.

Zimmer, U. & Yaramanci, U., 1993. In-situ Bestimmung der seismischen Dämpfung des Steinsalzes, *Kali Steinsaltz,* **11,** 168–174.